Optical Frequency Domain Reflectometry: sensing range extension and enhanced temperature sensitivity

by

Jia Song

Thesis submitted to the
Faculty of Graduate and Postdoctoral Studies
In partial fulfillment of the requirements for the

M.Sc. degree in Physics

Ottawa-Carleton Institute for Physics
University of Ottawa
Ottawa, Canada

To my family

Abstract

Optical fiber sensors have attracted tremendous attention over last two decades and have been successfully employed in various sensing applications, including temperature, strain, current, and so on. Among all types of optical fiber sensors, optical frequency domain reflectometry (OFDR) has been widely studied for its merits of simple configurations, high spatial resolution and high sensing accuracy. However, current limitation on OFDR lies in the sensing range and sensing accuracy. The state of art performance of commercial OFDR provides ~70m sensing range as well as 0.1K temperature accuracy. This is not adequate for large building distributed health monitoring due to the limited sensing range. Besides, high temperature response is also on demand for high precision measurement. To resolve the above limitation, in this thesis two major subjects have been studied regarding improving the performance and applicability of OFDR: One aims at extending the sensing range of OFDR while the other one focuses on enhancing temperature sensitivity of OFDR.

Firstly, we proposed novel data resampling approach regarding tuning nonlinearities of laser source to extend the sensing range. Commercial OFDR employs auxiliary interferometer (AI) to trigger data acquisition, where the maximum sensing range is limited to a quarter of the optical path difference (OPD) of AI according to Nyquist Sampling theorem. By employing the data resampling algorithm, the sensing range is no longer restricted by OPD and can even reach laser coherent length since OFDR is based on coherent detection scheme. Three data resampling algorithms are

individually discussed and a sensing range of ~300m (~4 times the sensing range of commercial OFDR) with 8cm spatial resolution is for the first time achieved.

Secondly, the temperature response of OFDR is enhanced and we successfully achieved high temperature accuracy distributed sensing. One advantage of high temperature response is to enhance the spatial resolution since less spatial points are required in performing cross-correlation, while the other advantage is to obtain high temperature accuracy measurement at the same spatial resolution compared to that of traditional OFDR. This is especially important for maintaining spatial resolution under long range OFDR sensing since the total wavelength tuning range is smaller than traditional OFDR. Commonly the temperature response of single mode fiber is contributed by both thermal expansion coefficient and thermal optic coefficient of the waveguide and can be enhanced by increasing either of those coefficients. Thermal expansion coefficient is related with material property and is a weighted value of both bare fiber and coating. By using a large thermal expansion coefficient acrylic plank as a "coating" on SMF, we achieved ~9 times temperature response (~95 pm/ ˚C) compared with SMF (~10 pm/ ˚C). Further experiment is demonstrated with small diameter taper on an acrylic plank "coating", in which case both thermal expansion coefficient and thermal optic coefficient are raised and a ~20 times temperature response than SMF (~200 pm/˚C) is obtained. This is especially meaningful for its easy fabrication, low cost and extremely high temperature response and leads to practical usage for high accuracy distributed temperature sensing.

Acknowledgement

It is my great honor to thank all people who have encouraged and helped me during my master's studies.

First of all, I would thank my supervisor, Professor Xiaoyi Bao for endowing me this opportunity to have my master study in her group. Prof. Bao, with her critical thinking, profound knowledge in physics and creative ideas, deeply impressed me. Her perseverance and dedication set me a good example for doing research. Her insightful instructions and valuable revisions helped and inspired me for fulfilling my research topics. This thesis would be impossible without her constant support and guidance. I would also express my gratitude to Professor Liang Chen, his precious help, meaningful suggestions and detailed revision helped improving the quality of this thesis.

Secondly, I shall thank Dr. Ping Lu for his detailed guidance, useful instructions and precise modification. I gained deep understanding in fiber optics and was able to find suitable research topics through discussions with him.

I also thank Dr. Wenhai Li for his efforts helping me with the OFDR configuration; this project cannot be fulfilled without whose early explorations.

Many thanks are given to Mr. Yanping Xu, who not only helped me in lab but also in daily lives. His strong motivation and optimism inspired me when I was low. I shall give special thanks to Yang Lu. His comments and advices helped improving the performance of OFDR system. I would also thank Dr. Zengguang Qin for his

meaningful instructions and assistance in research topics and daily lives.

I am thankful to all other colleagues in this lab: Dr. Chams Baker, Dr. Zhonghua Ou, Mr. Yang Li, Mr. Bhavaye Saxena, Dr. Meng Pang, Dr. Xiaozhen Wang, Dr. Dapeng Zhou, Ms. Daisy Williams, Ms. Meiqi Ren, Mr. Dao Xiang and Mr. Hugo Larocque.

Lastly, I shall sincerely thank my family and my best friends, for their support, anticipation, encouragement and comforts. I shall never forget your blessing and comforting me in those tough times, which set up my resolution to pursue this life.

I would also like to thank Collaborative Research and Training Experience Program (CREATE) program by Natural Sciences and Engineering Research Council of Canada (NSERC) that supported me for the entire master study.

Statement of originality

This work contains no material which has been accepted for the award of any other degree or diploma in any university or other tertiary institution and, to the best of my knowledge and belief, contains no material previously published or written by another person, except where due reference has been made in the text.

I give consent to this copy of my thesis, when deposited in the University Library, being available for loan and photocopying.

SIGNED: ……..

DATE: ……...

Supervisors: Prof. Xiaoyi Bao

Contents

List of Figures

List of Tables

List of Acronyms

AI	auxiliary interferometer
APC	angled polished connector
BOTDA	Brillouin optical time domain analysis
DAQ	data acquisition card
ESA	electrical spectrum analyzer
FBG	fiber Bragg gratings
FFT	fast Fourier transform
FMCW	frequency modulated continuous wave
FMCW SAR	frequency modulated continuous wave synthetic aperture radar
FP	Fabry–Pérot
FUT	fiber under test
FWHM	full width at half maximum
MZI	Mach-Zehnder interferometer
NU-FFT	non-uniform fast Fourier transform
OFDR	optical frequency domain reflectometry
OLCR	optical low coherence reflectometry
OPD	optical path difference
OTDR	optical time domain reflectometry
PBS	polarization beam splitter

PC	polarization controller
PD	photo detector
PDL	polarization dependent loss
RI	refractive index
SBS	stimulated Brillouin scattering
SMF	single mode fiber
SNR	signal-to-noise ratio
SVAA	slow-varying-amplitude-approximation
TLS	tunable laser source

Chapter 1
Introduction

1.1 Background and Motivation

Optical fibers have attracted tremendous attention ever since the first success fiber manufacturing process which reduced fiber loss to the acceptable level of 20dB/km by Corning in the 1970s. For the past 40 years, optical fibers have enjoyed great growth with multiple applications in high speed long distance communication systems, optics imaging, ultrafast lasing and optical sensors [1]. Thanks to the development in optoelectronics industry where the cost of optical components has been steadily reduced, fiber sensors gradually mature and exhibit significant advantages over traditional sensors. Fabricated in pure silica, the fiber is low-cost and is feasible to implement remote and distributed sensing with an immunity to electromagnetic interference and can survive in harsh environment. Another obvious advantage is the low transmission loss which guarantees the high signal to noise ratio (SNR) compared with that in electrical counterparts. Fiber is also sensitive to external perturbations like temperature, strain or vibration and can be calibrated to perform as a sensor, further applications like humidity sensing and chemical sensing are also feasible with special coating [2, 3]. Lastly, fibers are fabricated in a compact size with sub-millimeter diameter; this leads to its light-weight packaging and versatilities particularly in limited space and portable usages. These advantages made fiber a tool of choice in

sensing where many efforts have been done in various sensing applications.

Fiber optical sensors can be divided into two categories: point sensors and distributed sensors. Point sensor works at a specific area and is much similar to those electrical sensors where a separate channel is needed for each sensor. Generally, point sensors can be divided into two classes: Fiber Bragg Gratings (FBG) sensors and interferometer sensors. FBG is a sensing element written on fiber by UV exposure and reflects a resonant wavelength (Bragg wavelength) [4]. The Bragg wavelength is intrinsically temperature and strain sensitive and shifts proportionally with temperature and strain, or more generally any perturbations that modulate the refractive index or physical grating period. By sending a broad band light source into FBG and monitoring the resonant wavelength shift, the local temperature or strain can be extracted. Interferometer sensors are based on mode coupling theories where two (or more) modes propagating in fiber undergo different optical paths recombine at certain point. The recombined optical signal is a summation of all optical modes, changes like temperature or strain will have an effect on optical paths and result in optical wavelength shifts or power variation if a narrow line-width light source is implemented. To date, many interferometer sensors have been proposed including Sagnac interferometer, Fabry-Perot interferometer, Michelson interferometer and Mach-Zehnder interferometer, etc [3, 5-15]. On their own point sensors have a comparable performance over commonly used electrical sensors. An advantage over electrical sensors is the possibility to multiplex many of point sensors in series if each point sensor is designed to resonant at different central wavelength, in which way

only one channel is required to measure simultaneously. However, a multiplexed point sensors array is unable to detect any event that happens between two point sensors, which will eventually miss the event and therefore is named quasi-distributed sensor.

On the other hand, distributed sensors can function within the whole fiber length where no event will be missing, thus became a predominate approach to monitor health condition of large structures such as bridges, pipelines, oil wells, dams and other civil constructions for their compactness, real-time processing and high sensitivity. Several useful techniques have been developed over the past 20 years in distributed fiber sensors based on the measurement of intrinsic backscattering light, including Raman, Brillouin and Rayleigh scattering [1, 16-29] which are based on optical time domain reflectometry (OTDR), and coherent analysis including optical frequency domain reflectometry (OFDR) and optical low coherence reflectometry (OLCR) (Further details shall be discussed in a later chapter). Among all the distributed sensing techniques, OFDR has been given tremendous attention because its high spatial resolution and large dynamic range [30]. OFDR involves continuous frequency modulated optical signal which originated from Frequency Modulated Continuous Wave Synthetic Aperture Radar (FMCW SAR) and possess a huge gain of -100dB sensitivity and sub-millimeter resolution in Fresnel reflection locating under coherent detection scheme.

Much similar to FBG as discussed previously, OFDR can be treated as a series of weak FBGs where the whole fiber was divided into multiple segments. Each segment contains a range of spatial points with random Rayleigh backscattering, these “frozen”

Rayleigh backscattering profiles can be modeled as a weak Bragg grating with randomly varying period [31]. In the case of a FBG, the resonant wavelength is determined by grating period and effective refractive index, n. Any change in these parameters leads to resonant wavelength shift. The Rayleigh backscattering responds in the same manner: changes in refractive index or physical length lead to a resonant wavelength shift. By calibrating this wavelength shift, one may achieve distributed sensing, which functions as thousands of FBGs multiplexed. This is of significant importance where high precision and high spatial resolution are required, for example, in large civil structure health monitoring.

In the past 10 years, a number of applications based on OFDR has been demonstrated including optical communication network monitoring, and distributed temperature, strain, vibration, hydrogen and other sensing applications [15, 31-34]. Besides, OFDR has also been employed in fiber microstructure mode coupling, thermal and mechanical properties analysis [35-37].

The sensing range of OFDR is limited by the OPD of auxiliary interferometer due to Nyquist sampling theorem, while the spatial resolution is inversely proportional to the wavelength tuning range. For distributed sensing, a number of spatial points are employed in cross-correlation to obtain the wavelength shift induced by environmental variations. The larger the data set, the higher temperature or strain accuracy one could get. However, the data set cannot be infinitely large in order to maintain certain sensing spatial resolution. Therefore, an optimized centimeter sensing resolution and comparable sensing precision (10pm/°C for temperature

sensing and 1.2pm/με for strain sensing) with respect to FBG can be achieved using OFDR, with up to 70 meters in length [38]. However, in some uncommon cases like oil pipeline monitoring, long distance distributed sensing is required which cannot be met using current OFDR configuration, thus a long range distributed OFDR sensor is very much practically important. Besides, there are works that have requirements of high accuracy temperature discrimination, where current OFDR set-up only shows 0.1 ˚C accuracy. Taking account of above practical requirements, this thesis aims at studying the theory of OFDR and improving the performance of OFDR.

1.2 Thesis contribution

In this thesis, two major works are done regarding improving the performance and applicability of OFDR: One aims at extending the sensing range of OFDR, while the other focuses on enhancing temperature sensitivity of OFDR.

Firstly, we proposed three novel approaches to extend the working range of OFDR, and an extended sensing range OFDR with good temperature and strain accuracies is achieved. This is also the first time an OFDR without triggered data acquisition is employed in distributed sensing. Conventional OFDR uses an auxiliary interferometer, which is essentially an unbalanced Mach-Zehnder interferometer to trigger data acquisition. This is a good approach to mitigate laser tuning nonlinearities in tunable laser source (TLS) and to trigger equal frequency interval sampling, but a major drawback is its limited sensing range. The physical principle behind this is that

sensing range of OFDR is limited by optical path difference (OPD). According to Nyquist sampling theorem, the sensing length in main interferometer is a quarter of the length of OPD. However, this traditional OFDR set-up is not capable of long range sensing due to increasing errors in triggered signals. Since the trigger interferometer recovers the phase inaccurate at longer length due to the finite coherence length of the laser, this trigger signal will affect the wavelength recovery for OFDR sensing detection at far distance. When temperature or vibration change, the clock signal is easily affected and becomes uneven. As a result, the spatial location will be smeared at far end of sensing range due to accumulated environmental variations on the OPD of the triggered interferometer.

To resolve this problem, one possible approach is to monitor the instant nonlinear phase of TLS and rectify sampling data by algorithms. In this way, the unbalanced auxiliary interferometer functions to subtract the instant phase of TLS and a short length of OPD could be used to avoid environmental effects. The sensing range is therefore only limited by the laser coherence length which is much longer than that in traditional OFDR. In this thesis, we propose three different data resampling algorithms, namely Non-Uniform fast Fourier transform (NU-FFT), De-skew filter and Cubic spline interpolation, to rectify data affected by tuning nonlinearity. Working principles, simulation results and real data results are provided for NU-FFT and De-skew filter, where the limitations for each algorithm are also discussed. Cubic spline interpolation with high resampling accuracy is lastly employed and proved to be working with a large wavelength tuning range. To the best of our knowledge, this

is for the first time a ~300m sensing range is successfully achieved with good sensing accuracy, which is much longer than the sensing range of commercial OFDR (~70m).

Secondly, we aim to enhance the temperature sensitivity of OFDR. In principle, temperature sensitivity depends on temperature response with a typical value of 10pm/˚C and number of spatial points used in cross-correlation. A larger number of spatial points indeed correspond to higher accuracy, but at a cost of spatial resolution. Another possible approach is to enhance the thermal coefficient, which is a summation of thermal expansion coefficient and thermal optic coefficient. Thermal expansion coefficient is related with material property and is a weighted value of both bare fiber and coating, while the thermal optic coefficient describes refractive index as a function of temperature. The first trial we made is to glue bare fiber on a large thermal expansion coefficient acrylic plank, which functions as a "coating" and enhances the overall temperature response. The second trial is to glue an ultrathin taper on acrylic plank, in which case both thermal expansion coefficient and thermal optic coefficient shall be enhanced, due to the waveguide change induced by strain.

In the first trial, ~95pm/ ˚C and ~85.7pm/˚C temperature response are observed using acrylic (extruded) and acrylic (cast) plank, respectively. It is also possible to measure thermal expansion coefficient by using the same set-up if the plank is thick enough. In the second trial, an ultra-thin taper with 1μm diameter is attached on acrylic holder. The experiment demonstrates that, the thermal coefficient of taper with acrylic coating is ~200 pm/˚C, ~20 times more than the sensitivity of single mode fiber (SMF) as both thermal expansion coefficient and thermal optic coefficient contribute to its

temperature response.

This is especially significant as the sensitivity is for the first time being enhanced ~20 times. Besides, no expensive components are employed in this configuration, which leads to practical usage for high precision temperature measurement.

1.3 Thesis outline

This thesis contains five chapters and is organized as follows:

Chapter 1 states the background, motivation and contributions of this thesis.

Chapter 2 lists several reflectometers based on Rayleigh scattering including OTDR, OLCR and OFDR. A focus is given on OFDR where fundamental theory, working principles and limitations are discussed.

Chapter 3 proposes three novel approaches to extend the sensing range of OFDR. The working principles, algorithms, performances and analysis are provided and an extended range OFDR with good temperature and strain accuracies is achieved.

Chapter 4 studies the impacting factor in temperature sensing and aims at enhancing temperature sensitivity. A taper structure is employed and proved to be able to enhance temperature sensitivity where theoretical analysis and experimental results are described and discussed. Other potential approaches are also proposed (and experimentally proved).

Chapter 5 concludes all the work in this thesis and proposes possible approaches to improve performance and further applications of OFDR for future research.

Chapter 2

Distributed fiber sensor and principle of OFDR

2.1 Distributed fiber optical sensors

Fiber optical point sensors are widely used in sensing for their compactness and performance. However, a major problem occurs when an event happens between two point sensors, in which case this event will be undetected. On the other hand, distributed optical sensors can continuously work within the whole sensing range where no event undetected. This advantage enables distributed optical sensors to be most desirable for health monitoring of large structures such as bridges, pipelines, oil wells, dams and other civil constructions.

The distributed fiber optical sensors are realized by analyzing scattering light that occurs along the fiber. There are basically 4 types optical scattering when input light travels into gas, liquids and solids: Raman, Brillouin, Rayleigh and Rayleigh wing [39]. A typical spontaneous scattering spectrum from solid state matter is provided in the following figure.

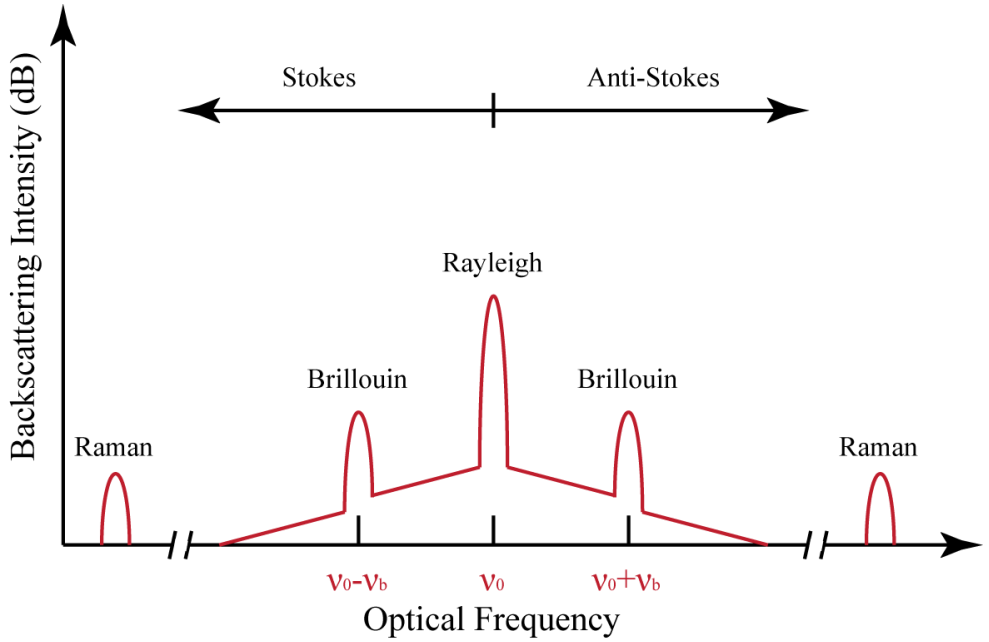

Fig. 2.1 Typical spontaneous scattering spectrum from solid state matter

When light is scattered from an atom (or molecule), most photons are elastically scattered. However, a small portion of the scattered light (approximately 1 in 10 million photons) is scattered by an excitation, with the scattered photons having a frequency different from the incident photons [39]. Raman scattering is induced by the interaction between light and vibration modes of the molecules in the scattering medium. Typically the vibration mode has a frequency of ~10^{12} to ~10^{14} Hz, which is the frequency shift from the input light. The intensity of Raman backscattering is a function of temperature [1, 39] and thus could be employed in distributed temperature sensing.

Brillouin scattering represents the interaction between light with propagating density waves or acoustic phonons. The acoustic phonon is generated through electrostriction and in turn modulates the refractive index of the medium [1, 39]. Brillouin scattering is also a nonlinear process, where the input frequency is shifted by Brillouin

frequency with a typical value of ~10GHz. The Brillouin frequency is intrinsically related to temperature and strain. Therefore by measuring the Brillouin frequency shift one could detect the local temperature or strain.

When applied to sensing, Raman and Brillouin based sensors show some common properties as they both use OTDR techniques. OTDR is originally used for estimating fiber length and overall attenuation, as well as fault locating [40]. By sending a laser pulse into the fiber under test (FUT) and measuring the backscattering Raman or Brillouin light, the distributed temperature or strain information could be obtained [16, 20, 26, 27]. Raman OTDR commonly measures the total power in Raman spectrum which is proportional to local temperature [16-18], while Brillouin OTDR measures the Brillouin spectrum by sweeping the Brillouin frequency using high speed oscilloscope or electrical spectrum analyzer (ESA) and the Brillouin frequency is obtained by fitting the Brillouin spectrum. Another commonly used distributed sensor based on Brillouin effect is Brillouin Optical Time Domain Analysis (BOTDA) where stimulated Brillouin scattering (SBS) is generated by interaction between pump light (from the end of fiber) and probe light (from the beginning of fiber).

The spatial resolution of OTDR is determined by the laser pulse-width [40]: a longer pulse-width improves dynamic range but at a cost of lower spatial resolution; a shorter pulse-width corresponds to a higher spatial resolution but the overall sensing length is limited. Typically, the state of art performance for those OTDR based distributed sensors is ~cm spatial resolution with ~km sensing length, and m spatial resolution with ~100km sensing length, with a temperature and strain accuracy of

~1˚C and ~10με, respectively [21, 24, 41-45].

2.1.1 Rayleigh Scattering based Distributed Sensor

Rayleigh scattering is known as the scattering of light from non-propagating density fluctuations or entropy fluctuations. Rayleigh wing scattering is induced by the fluctuations in the orientation of anisotropic molecules and has a broad spectrum but low scattering intensity [39]. Compared with Raman or Brillouin scattering, Rayleigh scattering is a linear process where frequency shift occurs.

Next we shall introduce mathematic treatment of Rayleigh scattering. Here we adopt the thermodynamic theory of light scattering. In this case, the light scattering occurs as the result of fluctuations in the dielectric constant and is a result of thermodynamic variables like material density and temperature. We take the density ρ and temperature T as independent thermodynamic variables, and express the fluctuation of dielectric constant as [39]:

$$\Delta\varepsilon = \left(\frac{\partial\varepsilon}{\partial\rho}\right)_T \Delta\rho + \left(\frac{\partial\varepsilon}{\partial T}\right)_\rho \Delta T \tag{2.1}$$

To a good accuracy of ~2%, the second term can be omitted since the dielectric constant depends more strongly on density than on temperature. Now we choose the entropy *s* and pressure *p* to be independent thermodynamic variables which affect the density. Then the variation in density $\Delta\rho$ can be expressed as:

$$\Delta\rho = \left(\frac{\partial\rho}{\partial p}\right)_s \Delta p + \left(\frac{\partial\rho}{\partial s}\right)_p \Delta s \tag{2.2}$$

Here the first term describes adiabatic density fluctuation (acoustic waves) which leads to Brillouin scattering. The second term describes isobaric density fluctuations (entropy fluctuations) and leads to Rayleigh scattering. The two contributions to $\Delta\rho$ are quite different in character as the equation describing Δp and Δs are different. The equation of motion describing Brillouin scattering leads to a Lorentzian lineshape, while the equation of motion describing Rayleigh shall be given as follows.

The equation describing entropy fluctuation Δs is found to be the same with that describing temperature variations [39]:

$$\rho c_p \frac{\partial \Delta s}{\partial t} - \kappa \nabla^2 \Delta s = 0 \tag{2.3}$$

Where c_p denotes the specific heat at constant pressure, κ denotes the thermal conductivity. This entropy fluctuation obeys a diffusion equation where a solution can be found:

$$\Delta s = \Delta s_0 e^{-\delta t} e^{-iq \bullet r} \tag{2.4}$$

Here, the damping rate of the entropy disturbance is given by $\delta = (\kappa / \rho c_p) q^2$. Unlike pressure waves, entropy waves do not propagate. The full width at half maximum (FWHM) of Rayleigh scattering is given by

$$\delta\omega_c = (4\kappa / \rho c_p) |k|^2 \sin^2(\theta / 2) \tag{2.5}$$

In the fiber, the only possible directions for scattering are forward ($\theta = 0$) and backward ($\theta = \pi$). For Rayleigh based sensing, like OTDR and OFDR (shall be discussed in following sections) only the backscattered light is detectable. Therefore, substituting $\theta = \pi$ into eq. 2.5, we get:

$$\delta\omega_c = (4\kappa / \rho c_p) |k|^2 \tag{2.6}$$

For silica, $\kappa = 13\text{mW}/\text{cm}^{-1}\text{K}$, $\rho = 2.648\text{g}/\text{cm}$, $c_p = 0.7\text{J}/\text{gK}$, taking all these parameters into account, a typical value of FWHM of Rayleigh backscattering light is 0.79MHz at 1550nm.

Over the last 20 years, Rayleigh backscattering based sensing has been proposed in 3 types [1], including optical time domain reflectometry (OTDR), optical low coherence reflectometry (OLCR) and optical frequency domain reflectometry (OFDR).

2.1.2 Optical Time Domain Reflectometry (OTDR)

OTDR [40] is the most commonly used distributed sensing means and has had a long history. Rayleigh OTDR is basically sending a pulsed laser into fiber under test and measures the backscattering Rayleigh reflection or Fresnel reflection using a photo detector (PD). After sending a series of pulses and averaging, the spatial information will be given. A typical set-up of OTDR is shown in following figure:

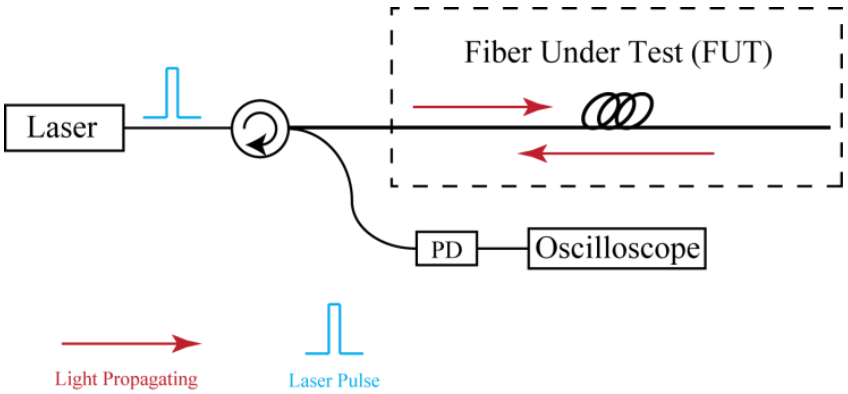

Fig. 2.2 Typical set-up of OTDR

Performance of OTDR

The spatial resolution is directly related to the pulse-width of the laser. Suppose the

laser has a pulse-width of time τ then it is impossible to distinguish the event within the pulse duration. This pulse duration corresponds to a spatial resolution $\Delta l = v_g \bullet \tau / 2$, where v_g is the group velocity in the fiber and with a typical value of $2\times10^8 \mathrm{m/s}$. A 10 ns pulse corresponds to roughly 1m spatial resolution. Following figure shows the typical OTDR trace from the oscilloscope.

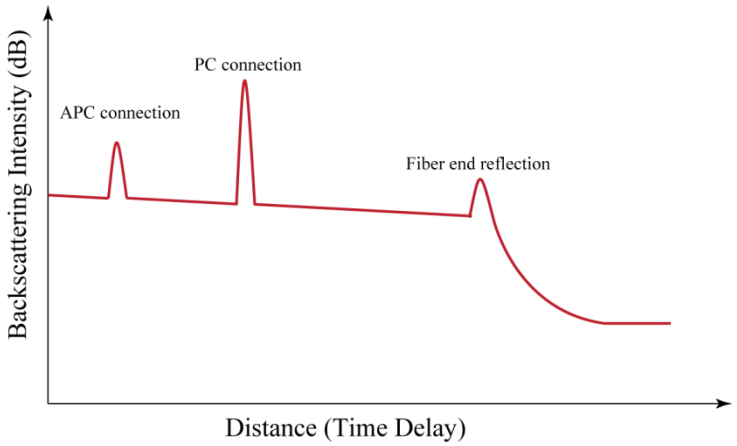

Fig. 2.3 Illustration of typical OTDR trace

There are several Fresnel reflections rather than Rayleigh backscattering, including angled polished connector (APC), polished connector and fiber end reflection. APC and PC are both used to connect fibers where APC is less reflective due to the angled polishing compared with PC. Commercially used fiber has an attenuation factor of ~0.2dB/km, which means the power drops 0.2dB after travelling through 1km length. The attenuation can also be calculated by fitting the slope of OTDR trace.

The dynamic range of OTDR is dependent on a combination of pulse power, pulse width and sensitivity of PD. A higher pulse power and longer pulse width will enhance SNR and sensing range but at a cost of spatial resolution. A shorter pulse width indicates a higher spatial resolution, while the sensing length and dynamic range is correspondingly limited.

Phase-sensitive OTDR in vibration sensing

Apart from attenuation and fault locating, OTDR has been applied to the distributed intrusion monitoring and vibration sensing [24, 46] by utilizing the interference effects within the narrow probe pulses by using a laser source with narrow line-width and stable frequency, which is named phase-sensitive OTDR. The configuration of phase-sensitive OTDR is similar to conventional OTDR, except for the narrow line-width laser source. Assuming that both the FUT and the laser source are stabilized which means that the statistical feature of Rayleigh scattering along the fiber length could be considered to be frozen, the time-domain traces will present a unique signature due to the interference effect. If a certain section of the fiber suffers from disturbance, the local refractive index would be modulated. As a result the Rayleigh spectrum receives a phase shift where the intensity of the interference spectrum will be changed. By measuring this intensity difference one could measure the disturbance; what's more, the distributed vibration event could also be measured by sending multiple pulses at a constant frequency. Currently, a ~1km sensing range with up to 1KHz vibration frequency could be achieved using phase-sensitive OTDR [45].

Performance of distributed sensors

Before I start the next chapter focusing on optical frequency domain reflectometry (OFDR), I shall present a comparison of state of art performance of all types of

distributed sensors.

Sensor type	Method	Usage	Spatial Res.	Sensing Range	Sensitivity
Phase OTDR	Rayleigh	Vibration & Intrusion	0.5m	124km [47]	3MHz for vibration [48]
Polarization OTDR	Rayleigh	Vibration	10m	1km[22]	5kHz
OFDR	Rayleigh	Temperature, Strain & vibration	1cm	70m [38]	0.1 ˚C 1με 30Hz

Table 2.1 Performance of various types of distributed Rayleigh fiber sensors

From the above table, we may find that phase OTDR and polarization OTDR sensors are both based on OTDR techniques, where the spatial resolution is limited by pulse-width of the laser. On the other hand, OFDR as a newly developed distributed sensor, has advantages like high spatial resolution (~1cm) and high sensitivity (~0.1˚C and ~1με), which is a great enhancement over OTDR based sensors. We shall discuss OFDR in the next section.

2.2 Theory of OFDR

2.2.1 Fundamental theory of OFDR with two electrical fields

In this section, a general set-up of OFDR is presented with the traditional set-up of OFDR. To help understand the mechanism behind OFDR, a recapitulative theoretical calculation with two electrical fields is provided [30].

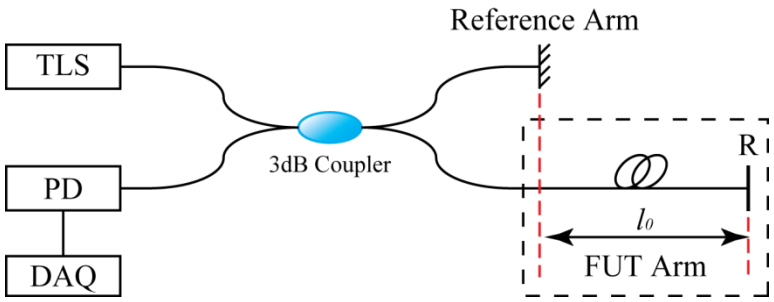

Fig. 2.4 Schematic set-up of traditional OFDR system

Following Fig. 2.4, a traditional OFDR set-up is illustrated. It consists of a tunable laser source (TLS), a 3dB coupler, a photo detector (PD), a data acquisition card (DAQ) and two fiber arms. The light from TLS undergoes the 3dB coupler and is divided into two arms: the reference arm and a fiber under test (FUT) arm. The lights from two different arms individually experience different optical path, returned from the reflectors, and recombined at the 3dB coupler. The recombined signal is then detected by PD and stored using a DAQ.

We start with an electrical field from the TLS, which has the form of the following:

$$E(t) = E_0 e^{i\varphi(t)} \tag{2.7}$$

where E_0 is the amplitude of the electrical field, $\varphi(t)$ is the phase term.

We also know that for a frequency modulated continuous wave (FMCW), there is a

relationship between modulated frequency and phase:

$$\varphi(t) = \int_0^t \omega(t)dt + \varphi_0 \tag{2.8}$$

For a single mode fiber, the chromatic dispersion for telecommunication optical wavelength, which is 1550nm, is typically 20ps/(nm*km). Taking identical wavelength sweeping range of 40nm and fiber length of 100m, the time delay induced by chromatic dispersion equals $20ps/(nm \bullet km) \bullet 40nm \bullet 0.1km = 8ps$, which corresponds to a length of $t_{delay} \bullet c / n_{eff} = 1.6mm$. This is quite a small value compared with the whole fiber length and thus the chromatic dispersion is negligible. To simplify the calculation, the initial point is set at the output of the 3dB coupler; also we ignore any attenuation effects in the fiber, where the electrical field at the reference arm can be expressed as:

$$E_r(t) = E_1 e^{i\varphi(t)} \tag{2.9}$$

The electrical field propagates and reflects at the mirror, and finally returned to the output port with a 3dB coupler. If the distance between the output port and the mirror is l_r, which corresponds to a time delay of τ_r, the electrical field can be expressed as:

$$E_r(t, \tau_r) = E_2 e^{i\varphi(t-2\tau_r)} \tag{2.10}$$

Similarly, the distance between the output port of 3dB coupler and a specific reflection point in FUT arm can be notified as $l_r + l_0$, where l_r is the same with the one in reference arm, and l_0 is the path difference between reference arm and FUT arm. The electrical field of FUT can be then expressed as:

$$E_{FUT}(t, \tau_r + \tau_0) = E_0 e^{i\varphi(t-2(\tau_r+\tau_0))} \tag{2.11}$$

The electrical fields then combine at the coupler and being detected by the PD at the other port. The electrical field at the detector can be expressed as:

$$\begin{aligned} E_d(t) &= E_r(t) + E_{FUT}(t) \\ &= E_1 e^{i\varphi(t-2\tau_r)} + E_2 e^{i\varphi(t-2(\tau_r+\tau_0))} \end{aligned} \tag{2.12}$$

The intensity of linearly polarized light can be represented as:

$$I(t) = < E_d(t)^2 > \propto E_d(t) \bullet E_d^*(t) \tag{2.13}$$

We then substitute Eq. (2.10) into Eq. (2.11), and the intensity can be expressed as:

$$\begin{aligned} I(t) &= (E_r(t) + E_{FUT}(t)) \bullet (E_r^*(t) + E_{FUT}^*(t)) \\ &= E_r(t) \bullet E_r^*(t) + E_{FUT}(t) \bullet E_{FUT}^*(t) + E_r(t) \bullet E_{FUT}^*(t) + E_{FUT}(t) \bullet E_{FUT}^*(t) \\ &= I_r(t) + I_{FUT}(t) + 2E_1E_2 \cos\{\varphi(t-2\tau_r) - \varphi(t-2(\tau_r+\tau_0))\} \\ &= I_r(t) + I_{FUT}(t) + 2\sqrt{I_r(t)I_{FUT}(t)} \cos\{\varphi(t-2\tau_r) - \varphi(t-2(\tau_r+\tau_0))\} \end{aligned} \tag{2.14}$$

Since the two electrical fields are from the same source, within the coherence length the two electrical fields are correlated. Eq. (2.14) can be further simplified if we introduce the visibility:

$$I(t) = I_0\{1 + V\cos\{\varphi(t-2\tau_r) - \varphi(t-2(\tau_r+\tau_0))\}\} \tag{2.15}$$

here $V = 2\sqrt{I_r I_{FUT}} / (I_r + I_{FUT})$ is the visibility of the interference pattern while $I_0 = I_r + I_{FUT}$. The visibility found its maximum value when $I_r = I_{FUT}$.

If the wavelength is linearly tuned which is the case in OFDR system, as shown below:

$$\varphi(t) = \int_0^t \omega(t)dt = \int_0^t (\gamma t + \omega_0)dt = \frac{1}{2}\gamma t^2 + \omega_0 t + \varphi_0 \tag{2.16}$$

here $\omega(t) = \gamma t + \omega_0$ is a linearly tuning frequency, γ the optical frequency tuning speed, ω_0 the initial optical frequency. φ_0 is the initial phase from the TLS.

Then the interference term in Eq. (2.15) is reduced to:

$$I(t) = I_0\{1 + V\cos\{\gamma\tau_0(2t - 2(2\tau_r + \tau_0)) + 2\varpi_0\tau_0\}\} \tag{2.17}$$

Note τ_r is some time delay which has no contribution to the intensity, therefore can be intentionally ignored. Finally the following formula can be obtained:

$$I(t) = I_0\{1+V\cos\{2\gamma\tau_0 t + 2\varpi_0\tau_0 - 2\gamma\tau_0\tau_0\}\} \quad (2.18)$$

From the above derivation, it is found that one specific location which has a distance of l_0 (and a time delay of τ_0) towards reference point corresponds to a beat frequency of $2\gamma\tau_0$. By performing an FFT, the beat frequency can be extracted and viewed from the frequency spectrum. Therefore, OFDR system is able to monitor reflection points within FUT and enjoys merits like high spatial resolution, quick measurement and so on.

Please note that in the above derivation, only two electrical fields are calculated. This is a good approximation for a strong reflection point in FUT, like PC connector or mirror. However, in real OFDR measurement, the electrical field in $E_{FUT}(t)$ is a summation of all Rayleigh backscattering points within the fiber, thus cannot be represented by the general idea above. This derivation did present general understanding on how OFDR functions, however it is not rigorous to be a theoretical derivation. In the following section, a detailed derivation treating multiple electrical fields interference shall be given.

2.2.2 Fundamental Theory of OFDR with polarization diversity scheme

In this section, the fundamental theory of OFDR shall be discussed with actual experimental set-up and an analytical solution shall be given. Both ideal linear

frequency modulation and actual frequency modulation with nonlinearity are discussed in details.

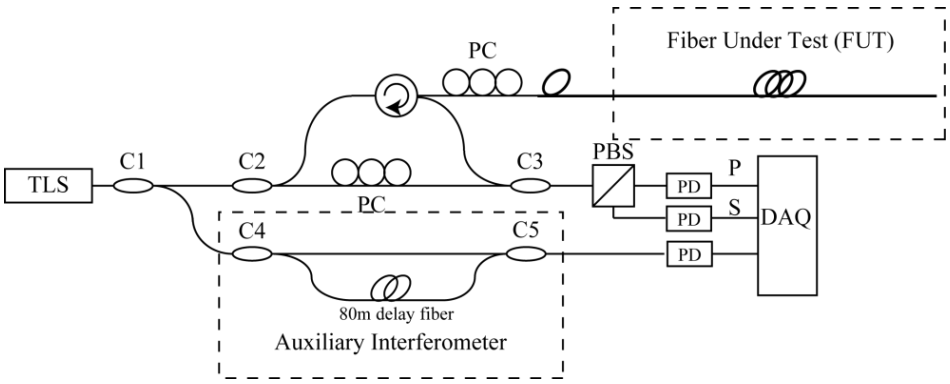

Fig. 2.5 Illustration of OFDR set-up with polarization diversity scheme

To start, a schematic illustration of OFDR set-up is exhibited in Fig. 2.5. The configuration of the OFDR system consists of a tunable laser source (TLS), a main interferometer with a polarization beam splitter (PBS) based polarization diversity receiver, an auxiliary interferometer with a length of optical path delay (OPD) to measure instantaneous optical frequency, photo detectors (PDs) and a data acquisition card (DAQ).

Light from TLS is split into two portions at the first coupler (marked as C1), 99% power is sent into the main interferometer while 1% power is sent into auxiliary interferometer. In main interferometer, half the light from C2 enters a circulator, PC and finally the fiber under test (FUT). The spontaneous Rayleigh backscattered light from FUT combines with the other light from C2 at the coupler C3 and then split into two orthogonal polarization components by a PBS and is detected by two PDs. The auxiliary interferometer is implemented either as a trigger signal or a measurement of instant optical frequency. In both ways, the auxiliary interferometer is used to mitigate the tuning nonlinearity which may severely deteriorate the spatial resolution. However,

in this section we shall mainly focus on the mechanisms of OFDR, where an ideal perfect linear tuning frequency is assumed, the compensation for tuning nonlinearity shall be discussed in next section.

As shown in Fig. 2.5, the TLS has an optical frequency $\omega(t)$ and a phase of $\varphi(t)$. The light from coupler C2 is set as the zero point. The electrical field can be expresses as [49]:

$$E(t) = E_0(t)e^{i\varphi(t)} \tag{2.19}$$

where $E_0(t)$ is the amplitude of the electrical field.

If the light propagates a distance of l , the electrical field can be written as:

$$E(\tau,t) = \frac{A}{\sqrt{2}} E_0(t-\tau)e^{i\varphi(t-\tau)}e^{-\alpha l} \tag{2.20}$$

where τ is the time delay and is proportional to l: $\tau = l/V = l/(c/n_g)$, V is the group velocity and n_g is the group refractive index. A is a complex number describing phase shift that undergoes a coupler or a circulator, α is the attenuation coefficient.

The electrical field at one arm of the main interferometer can be then expressed as follows:

$$E(\tau_b,t) = \frac{A_b}{\sqrt{2}} E_0(t-\tau_b)e^{i\varphi(t-\tau_b)}e^{-\alpha l_b} \tag{2.21}$$

where τ_b corresponds to time delay from C2 to C3, l_b corresponds to the distance from C2 to C3.

If we look at a specific position z' at FUT, where a spontaneous Rayleigh backscattering light is generated and undergoes the circulator and finally reaches the

coupler C3, there are in total 4 fiber sections that have made contributions to electrical field: C2 to circulator, circulator to z' , Rayleigh backscattering light from z' to Circulator and Circulator to coupler C3. To simplify the calculation, the circulator is intentionally set as zero point, and all other leading fiber sections are considered to be length l_a (including C2 to circulator, and circulator to C3). In this way, the electrical field at z' can be expressed as:

$$E(\tau_{z'},t)=\frac{A_{z'}}{\sqrt{2}}E_0(t-\tau_{z'})e^{i\varphi(t-\tau_{z'})}e^{-\alpha l_{z'}} \tag{2.22}$$

The Rayleigh backscattering light returned to circulator is:

$$E(2\tau_{z'},t)=r(z')\frac{A_{2z'}}{\sqrt{2}}E_0(t-2\tau_{z'})e^{i\varphi(t-2\tau_{z'})}e^{-2\alpha l_{z'}} \tag{2.23}$$

where $r(z')$ is the local Rayleigh backscattering coefficient which is induced by local density fluctuation and is only related to position.

The light arrives at coupler C3 can be written as:

$$E(2\tau_{z'}+\tau_a,t)=r(z')\frac{A_{z'}}{\sqrt{2}}E_0[t-(2\tau_{z'}+\tau_a)]e^{i\varphi[t-(2\tau_{z'}+\tau_a)]}e^{-\alpha(2l_{z'}+l_a)} \tag{2.24}$$

Within the whole FUT, each Rayleigh scattering point shall be treated as an individual reflector and the electrical fields at coupler C3 is a summation of all Rayleigh backscattering points, which is:

$$E_a(t)=\frac{A_a}{\sqrt{2}}\sum_{z'}\{r(z')E_0[t-(2\tau_{z'}+\tau_a)]e^{i\varphi[t-(2\tau_{z'}+\tau_a)]}e^{-\alpha(2l_{z'}+l_a)}\} \tag{2.25}$$

Note A_a here denotes the total phase shift light travels through the FUT arm.

At the output port of coupler C3, the electrical field can be calculated by a jones matrix as:

$$
\begin{aligned}
E(t) &= E_a(t) + iE_b(t) \\
&= \frac{A_a}{\sqrt{2}} \sum_{z'} \{ r(z') E_0[t - (2\tau_{z'} + \tau_a)] e^{i\varphi[t-(2\tau_{z'}+\tau_a)]} e^{-\alpha(2l_{z'}+l_a)} \} \\
&\quad + i \frac{A_b}{\sqrt{2}} E_0(t - \tau_b) e^{i\varphi(t-\tau_b)} e^{-\alpha l_b}
\end{aligned}
\tag{2.26}
$$

To eliminate the polarization dependent loss (PDL), a polarization diversity measurement is implemented where two orthogonal components, P and S are split from a PBS and shown as follows:

$$
\begin{aligned}
E_p(t) &= \hat{P} \frac{T_p e^{i\varphi_p}}{2} \{ A_a \sum_{z'} \{ r_p(z') E_0[t - (2\tau_{z'} + \tau_a)] e^{i\varphi[t-(2\tau_{z'}+\tau_a)]} e^{-\alpha(2l_{z'}+l_a)} \} \\
&\quad + i \frac{A_b}{\sqrt{2}} E_0(t - \tau_b) e^{i\varphi(t-\tau_b)} e^{-\alpha l_b} \} \\
E_s(t) &= \hat{S} \frac{T_s e^{i\varphi_s}}{2} \{ A_a \sum_{z'} \{ r_s(z') E_0[t - (2\tau_{z'} + \tau_a)] e^{i\varphi[t-(2\tau_{z'}+\tau_a)]} e^{-\alpha(2l_{z'}+l_a)} \} \\
&\quad + i \frac{A_b}{\sqrt{2}} E_0(t - \tau_b) e^{i\varphi(t-\tau_b)} e^{-\alpha l_b} \}
\end{aligned}
\tag{2.27}
$$

where $\hat{P}$ and $\hat{S}$ denotes the vector of p and s components, T_p and T_s the split portion of PBS, φ_p and φ_s the phase shift in PBS, r_p and r_s the individual Rayleigh backscattering coefficients.

If we look at the p-detector, the received signal can be expressed as:

$$
I_p(t) = E_p(t) \bullet E_p^*(t) \tag{2.28}
$$

The DC portion of $I_p(t)$ is abandoned as no spatial information is contained, the AC portion of $I_p(t)$ can be then expressed as:

$$
\begin{aligned}
I_p^{AC}(t) &= \frac{T_p^2 A_a A_b^*}{4} \sum_{z} \{ e^{-\alpha(2l_{z'}+l_a+l_b)} r_p(z') E_0[t - (2\tau_{z'} + \tau_a)] E_0^*(t - \tau_b) \\
&\quad * e^{i\{\varphi[t-(2\tau_{z'}+\tau_a)]-\varphi(t-\tau_b)\}} \} + c.c.
\end{aligned}
\tag{2.29}
$$

where $c.c.$ denotes a complex conjugate of the first term in Eq. (2.29).

To have a more general idea of how OFDR functions, a perfect linearly tuning

frequency is assumed and the relationship between the phase and the optical frequency is:

$$\varphi(t)=\int_0^t \omega(t)dt=\int_0^t(\gamma t+\omega_0)dt=\frac{1}{2}\gamma t^2+\omega_0 t+\varphi_0 \tag{2.30}$$

where $\omega(t)=\gamma t+\omega_0$ is a linear tuning frequency, γ the optical frequency tuning speed, ω_0 the initial optical frequency. φ_0 here is the initial phase from the TLS. Therefore the phase term $\varphi[t-(2\tau_{z'}+\tau_a)]-\varphi(t-\tau_b)$ in Eq. (2.30) can be simplified as follows:

$$\begin{aligned}\varphi[t-(2\tau_{z'}+\tau_a)]-\varphi(t-\tau_b)=&\frac{1}{2}\gamma(\tau_b-\tau_a-2\tau_{z'})[2t-(2\tau_{z'}+\tau_a+\tau_b)]\\&+\omega_0(\tau_b-\tau_a-2\tau_{z'})\end{aligned} \tag{2.31}$$

The Eq. 2.32 can be further simplified if $\tau_a=\tau_b=\tau_0$ (corresponding to l_0), which is reasonable since τ_a and τ_b are merely some constant time delays which shall not have any effect on spatial information. Therefore the phase term is:

$$\varphi[t-(2\tau_{z'}+\tau_a)]-\varphi(t-\tau_b)=-2\gamma\tau_{z'}[t-(\tau_{z'}+\tau_0)]-2\omega_0\tau_{z'} \tag{2.32}$$

And the Eq. (2.29) is reduced to:

$$\begin{aligned}I_p^{AC}(t)=&\frac{T_p^2A_aA_b^*}{4}\sum_z\{e^{-\alpha(2l_{z'}+2l_0)}r_p(z')E_0[t-(2\tau_{z'}+\tau_0)]E_0^*(t-\tau_0)\\&\bullet e^{-i\{2\gamma\tau_{z'}[t-(\tau_{z'}+\tau_0)]+2\omega_0\tau_{z'}\}}\}+c.c.\end{aligned} \tag{2.33}$$

We then assume the output of TLS is stable, which means $E_0[t-(2\tau_{z'}+\tau_0)]\approx E_0(t)$, and $E_0^*(t-\tau_0)\approx E_0^*(t)$, then the Eq. (2.33) can be further simplified to:

$$\begin{aligned}I_p^{AC}(t)=&\frac{T_p^2A_aA_b^*}{4}\sum_z\{e^{-\alpha(2l_{z'}+2l_0)}r_p(z')E_0(t)E_0^*(t)\\&\bullet e^{-i\{2\gamma\tau_{z'}[t-(\tau_{z'}+\tau_0)]+2\omega_0\tau_{z'}\}}\}+c.c.\end{aligned} \tag{2.34}$$

Here, we introduce two normalization factors, $\varphi_p(z')$ indicating the local Rayleigh backscattering phase shift for the p-component and $m_p(t)$, indicating the amplitude

of all other constant parameters. $\varphi_p(z')$ and $m_p(t)$ are given as:

$$\varphi_p(z') = 2\tau_{z'}[\omega_0 - \gamma\tau_{z'}(\tau_{z'} + \tau_0)] - \vartheta_{rp(z')}$$

$$m_p(t) = |m_p(t)|e^{i\theta_p(t)} = \frac{T_p A_a A_b^*}{4}|E_0(t)|^2 \tag{2.35}$$

A compact form of Eq. (2.34) can be found as follows:

$$\begin{aligned} I_p^{AC}(t) &= \sum_{z'}\{|r_p(z')|\bullet|m_p(t)| \\ &\quad \bullet e^{-i\{2\gamma\tau_{z'}t + 2\tau_{z'}[\omega_0 - \gamma\tau_{z'}(\tau_{z'}+\tau_0)]\} + \vartheta_p(t) - \vartheta_{rp(z')}}\} + c.c. \\ &= 2\sum_{z'}\{|r_p(z')|\bullet|m_p(t)|e^{-2\alpha(l_{z'}+l_0)} \\ &\quad \bullet\cos(2\gamma\tau_{z'}t + 2\tau_{z'}[\omega_0 - \gamma\tau_{z'}(\tau_{z'}+\tau_0)] + \vartheta_p(t) - \vartheta_{rp(z')})\} \\ &= 2\sum_{z'}\{|r_p(z')|\bullet|m_p(t)|e^{-2\alpha(l_{z'}+l_0)} \\ &\quad \bullet\cos(2\gamma\tau_{z'}t + \vartheta_p(t) + \varphi_p(z'))\} \\ &= \sum_{z'}\{m_p(t,z')\bullet\cos(2\gamma\tau_{z'}t + \vartheta_p(t) + \varphi_p(z'))\} \end{aligned} \tag{2.36}$$

where $r_p(z') = |r_p(z')|e^{i\theta_{rp}(z')}$ is the local Rayleigh backscattering strength for p-component. $m_p(t,z') = 2|r_p(z')|\bullet|m_p(t)|e^{-2\alpha(l_{z'}+l_0)}$ is the normalized field strength. By applying slow-varying-amplitude-approximation (SVAA), $m_p(t,z')$ and $\vartheta_p(t)$ are time-invariant and $m_p(t,z') \simeq m_p(z')$, $\vartheta_p(t) \approx 0$. Finally the Eq. 2.36 is reduced to:

$$I_p^{AC}(t) = \sum_{z'} m_p(z') * \cos(2\gamma\tau_{z'}t + \varphi_p(z')) \tag{2.37}$$

Eq. 2.37 describes the received signal with respect to local Rayleigh backscattering profile, which is a summation of all Rayleigh backscattering points along the fiber and the time delay $\tau_{z'}$. If a complex Fourier transform is applied to Eq. (2.37), we may find:

$$
\begin{aligned}
I_p^{AC}(\omega) &= F(I_p^{AC}(t)) \\
&= \frac{\sqrt{2}\pi}{2}\sum_{z'} m_p(z')\left[e^{i\varphi_p(z')}\delta(\omega-2\gamma\tau_{z'})+e^{-i\varphi_p(z')}\delta(\omega+2\gamma\tau_{z'})\right]
\end{aligned}
\tag{2.38}
$$

Since $\omega > 0$, the second term in Eq. 2.38 is neglected and an intuitive form of distributed Rayleigh backscattering profile is provided:

$$
\begin{aligned}
I_p^{AC}(\omega) &= \frac{\sqrt{2}\pi}{2}\sum_{z'} m_p(z')e^{i\varphi_p(z')}\delta(\omega-2\gamma\tau_{z'}) \\
&= \sum_{z'}\kappa_p(z')\delta(\omega-2\gamma\tau_{z'})
\end{aligned}
\tag{2.39}
$$

where $\kappa_p(z') = \frac{\sqrt{2}\pi}{2} m_p(z')e^{i\varphi_p(z')}$ is a coefficient and is only related to local Rayleigh backscattering strength. $\delta(\omega-2\gamma\tau_{z'})$ is an impulse function which indicates a specific frequency (beat frequency) directly related to a position along the fiber. By analyzing the frequency, the local scattering amplitude could be easily observed.

The s-component from PBS could be derived similarly as well as the complex Fourier transform. A polarization independent signal can be then obtained by adding p and s components together which goes like follows:

$$
I^{AC}(t) = \sum_{z'} m(z')\bullet\cos(2\gamma\tau_{z'}t+\varphi(z'))
\tag{2.40}
$$

And in the frequency domain:

$$
\begin{aligned}
I^{AC}(\omega) &= \frac{\sqrt{2}\pi}{2}\sum_{z'} m(z')e^{i\varphi(z')}\delta(\omega-2\gamma\tau_{z'}) \\
&= \sum_{z'}\kappa(z')\delta(\omega-2\gamma\tau_{z'})
\end{aligned}
\tag{2.41}
$$

From the above derivation, we theoretically analyzed the electrical field at PD and through a Fourier transform, the frequency is found to be corresponding to local position and the amplitude at which the frequency corresponds to the scattering

amplitude. Since a polarization diversity approach is implemented, the polarization will have no effect on Rayleigh backscattering amplitude.

2.2.2.1 External Triggering in frequency domain treating tuning nonlinearities

In the previous derivation, it is assumed that the tuning frequency is in a perfect linear relationship with time, $\omega(t) = \gamma t + \omega_0$. However, this is not the case for any TLSs on the market. Most TLSs employ a Fabry–Pérot (FP) etalon (or similar mode-selection approaches), where the center wavelength is tuned by cavity length of the FP. The cavity length can be either tuned by a DC motor for coarse-tuning or a piezoelectric actuator for fine-tuning, but neither approach can provide linear tuning due to jitters in mechanical parts, which may induce phase noise in lasing procedure. Luckily, some previous work has been done by U. Glombitza and E. Brinkmeyer in their paper [49].

If we have a look at Eq. (2.41), where $I^{AC}(\omega) = \sum_{z'} \kappa(z')\delta(\omega - 2\gamma\tau_{z'})$, one specific frequency $\omega = 2\gamma\tau_{z'}$ corresponds to a specific position $\tau_{z'}$. The frequency tuning speed $\gamma = \gamma(t)$ is not a constant due to tuning nonlinearities, which means $\omega = 2\gamma(t)\tau_{z'}$ is not linear with $\tau_{z'}$ anymore.

If we recombine the electrical field, and expand it into Fourier series as follows:

$$E(t) = \int_{-\infty}^{+\infty} e_0(\nu)\exp(2\pi i\nu t)d\nu \tag{2.42}$$

where $\nu = \frac{1}{2\pi}\omega = \frac{1}{2\pi}\frac{d\varphi}{dt}$ is the instantaneous optical frequency. The light that

propagates to a specific position and then returns will induce a phase shift $\exp(i\beta(\nu)2l_{z'})$ where $\beta(\nu)$ is the propagation constant and z' is the position of Rayleigh scattering point. Combining them together, we may find:

$$E(t)=\int_{-\infty}^{+\infty} e_0(\nu)\exp[i\beta(\nu)2l_{z'}]\exp(2\pi i\nu t)d\nu \tag{2.43}$$

The propagation constant can be approximated as $\beta(\nu)=\beta(\nu_0)+\beta'(\nu_0)(\nu-\nu_0)$. The first term $\beta(\nu_0)$ is related with phase delay τ_{ph} and second term $\beta'(\nu_0)$ is related with group delay τ_{gr}. With some procedures omitted, the beat signal can be calculated as follows [49]:

$$I=I_0\left[1+\sum_{n=1}^{N}\{|r_{eff}|_n^2+2|r_{eff}|_n\cos(\varphi(t)-\varphi(t-\tau_{gr})+2\pi\nu_0(\tau_{ph}-\tau_{gr})+\varphi_0)\}\right] \tag{2.44}$$

here r_{eff} is some reflection factor. Remember $\varphi(t)-\varphi(t-\tau_{gr})\approx\tau_{gr}d\varphi/dt=\tau_{gr}2\pi\nu$ where higher order terms are negligible. Substituting $\varphi(t)-\varphi(t-\tau_{gr})=\tau_{gr}2\pi\nu$ into above equation, a more simplified version can be found:

$$I=I_0\left[1+\sum_{n=1}^{N}\{|r_{eff}|_n^2+2|r_{eff}|_n\cos(\tau_{gr}2\pi\nu+\varphi_0')\}\right] \tag{2.45}$$

where $\varphi_0'=2\pi\nu_0(\tau_{ph}-\tau_{gr})+\varphi_0$ is a summation of all constants. By taking the AC portion of beat signal, finally the equation is reduced to:

$$I=I_0\sum_{n=1}^{N}2|r_{eff}|_n\cos(\tau_{gr}2\pi\nu+\varphi_0') \tag{2.46}$$

From Eq. 2.46, we may find the time delay can be accurately measured whatever the frequency tunes, provided the instantaneous optical frequency measured properly. Each frequency ν corresponds to a specific τ_{gr}. If the signal was sampled at even time interval Δt, the frequency interval $\Delta\nu$ is not equal due to the tuning

nonlinearity. As a result, the spatial resolution will deteriorate to some extent, depending on how nonlinear the tuning process is.

As previously stated, the equal frequency interval $\Delta\nu$ could provide accurate time delay from FUT. One smart approach to achieve this is by employing an unbalanced Mach-Zehnder interferometer (MZI) as an external trigger, which has been shown on Fig. 2.5 as an auxiliary interferometer.

The analysis on auxiliary MZI is similar to that in main interferometer, two arms of MZI undergo different optical paths and result in a time delay τ_d:

$$\begin{aligned} E_1(t) &= E_0 e^{i\varphi(t)} \\ E_2(t) &= E_0 e^{i\varphi(t-\tau_d)} \end{aligned} \tag{2.47}$$

The interference signal at the output of MZI is:

$$\begin{aligned} I &\propto (E_1(t)+E_2(t))\bullet(E_1(t)+E_2(t)) \\ &\propto \cos(\varphi(t)-\varphi(t-\tau_d)) \end{aligned} \tag{2.48}$$

Considering a non-perfect linear sweep, the frequency tuning speed is not a constant:

$$\varphi(t)=\int_0^t \omega(t)dt=\int_0^t (\gamma(t)\bullet t+\omega_0)dt \tag{2.49}$$

Therefore the interference signal is:

$$\begin{aligned} I &= \cos\{\int_0^t (\gamma(t)\bullet t+\omega_0)dt-(\gamma(t-\tau_d)\bullet(t-\tau_d)+\omega_0)dt\} \\ &= \cos\int_0^t [(\gamma(t)-\gamma(t-\tau_d)]\bullet t+\gamma(t-\tau_d)\tau_d)]dt \end{aligned} \tag{2.50}$$

Their first term $[(\gamma(t)-\gamma(t-\tau_d)]\bullet t$ is negligible since $\gamma(t)\approx\gamma(t-\tau_d)$, and:

$$I=\cos(\int_0^t \gamma(t)\tau_d dt) \tag{2.51}$$

Since the auxiliary interferometer is employed as a rising-edge trigger, the corresponding frequency interval is therefore a constant.

2.2.2.2 Laser Linewidth Effect on Sensing Range

As being derived from the following section 2.2.4.1, it is found that the maximum sensing range is a quarter of the optical path difference from the auxiliary interferometer. However, OPD cannot be infinitely extended as one must keep a high contrast beat signal, which is then employed to trigger data acquisition in main interferometer. In this case, laser linewidth plays a dominant role. Laser linewidth is defined as the spectral linewidth of the laser, and is used to calculate coherent length. If the OPD is close or beyond laser coherent length, the beat signal is averaged out and the phase information to recover the instantaneous optical frequency deviates from real value, which then leads to a high temperature and strain uncertainty; this is a fundamental limit for triggered interferometer OFDR. Therefore, in triggered OFDR configuration, the sensing range is in principle limited by the laser coherent length with a maximum value of a quarter of laser coherent length. Typical OFDR products on market only possess a sensing range of 70m [38]. However, the sensing range can be ultimately close to coherence length, if it is not triggered by an auxiliary interferometer, further details shall be discussed in Chapter 3.

2.2.3 Distributed Temperature and Strain sensing based on OFDR

OFDR is primarily used to characterize and analyze network and optical waveguides until 1998, where local Rayleigh profile is found to have similarities with fiber Bragg gratings (FBG). This unique property is then employed in distributed temperature and strain sensing. In this section, the principles of distributed temperature and strain sensing based on local Rayleigh backscattering profile are discussed.

Weak FBG Model of OFDR

In previous sections, we have learned that the local Rayleigh backscattering profile along the fiber is obtained through a fast Fourier transform (FFT) and could be implemented in analyzing the optical networks, e.g. detecting fault position, where usually large scattering amplitude exists. However, the Rayleigh backscattering profile is also feasible for other applications since Rayleigh backscatter in optical fiber is caused by random fluctuations in the index profile along the fiber length. For a given fiber, the Rayleigh scattering amplitude as a function of distance is random but static, thus can be modeled as a weak FBG with random period [50]. This "Rayleigh" FBG is weak in amplitude but stable in different locations. To have a better understanding on principles of OFDR sensing, firstly we may recall the formula concerning central wavelength, or the Bragg wavelength of FBG [4]:

$$\lambda_B = 2n_e\Lambda \tag{2.52}$$

where n_e is the effective refractive index (RI) in the fiber core and Λ is the grating

period. The effective refractive index quantifies the velocity of propagating light as compared to its velocity in vacuum. n_e not only depends on the optical wavelength, but also depends on the specific optical mode that propagates. For a multimode fiber, as thousands of modes propagate in the fiber, n_e is a summation of all weighted modes with different effective RIs.

A FBG is sensitive to environmental variations like temperature and strain, the relative Bragg wavelength shift of a FBG due to temperature or strain change is given by [4]:

$$\Delta\lambda / \lambda = C_\varepsilon \varepsilon + C_T \Delta T \tag{2.53}$$

where C_ε is some coefficient of strain, and $C_T = \alpha_\Lambda + \alpha_n$ is the thermal coefficient. C_T consists of two terms: α_Λ is the thermal-expansion coefficient, which is induced by grating period change, α_n is the thermal-optic coefficient, which is induced by the effective RI change. A simple explanation can be found by differentiating both sides of Eq. (2.53), with respect to temperature T:

$$\Delta\lambda_B(T) = 2\{\Delta n_e(T)\Lambda + n_e \Delta\Lambda(T)\} \tag{2.54}$$

Apparently $\Delta n_e(T)$ contributes to α_n and $\Delta\Lambda(T)$ contributes to α_Λ.

In the above discussions, it is found that the FBG spectral response is sensitive to temperature and strain. The distributed Rayleigh backscattering presents some similar properties: changes in refractive index or physical length shift the reflected spectrum in frequency. The physical length (or average grating period of Rayleigh backscattering profile) and refractive index of the fiber are intrinsically sensitive to environmental perturbations like temperature and strain. It is even possible for sensing

humidity (provided the fiber coating is hydrophilic) and, electromagnetic fields [31].

The wavelength shift $\Delta\lambda$, or frequency shift $\Delta\nu$, of the backscatter pattern due to a temperature change, ΔT, or strain along the fiber axis, ε, is identical to the response of a fiber Bragg grating:

$$\Delta\lambda / \lambda = -\Delta\nu / \nu = K_T \Delta T + K_\varepsilon \varepsilon \tag{2.55}$$

here K_T is a summation of thermal-expansion coefficient α_Λ and thermal-optic coefficient α_n, with typical values of $0.55\times10^{-6}\,°C^{-1}$ and $6.1\times10^{-6}\,°C^{-1}$, respectively. For α_Λ, if the fiber is coated with coating, α_Λ is a summation of weighted thermal-expansion coefficients of both bare fiber and coating materials where α_Λ is slightly larger than that of single mode fiber.

K_ε is the strain coefficient and is a function of refractive index n_e, strain-optic tensor, p_{ij}, and Poisson's ratio, μ. Typical values given for n, p_{12}, p_{11} and μ for germanium-doped silica yield a value for K_ε of 0.787.

Therefore, OFDR could perform as a distributed sensor in the entire fiber length by simply calibrating the wavelength shift for both temperature and strain in a moderate range (larger perturbations will induce slight nonlinearities as $\Delta\lambda$ is wavelength dependent).

2.2.4 Sensing resolution vs. spatial resolution

In the above section, the mechanism of OFDR sensing is reviewed. In this section we shall introduce some further discussion on sensing length, spatial resolution, sensing

accuracy and sensing resolution.

2.2.4.1 Spatial Resolution

Firstly, we shall introduce the spatial resolution of OFDR system and a derivation shall be given in later section. The spatial resolution Δz is determined by frequency bandwidth of the scanning range from the following equation:

$$\Delta z = c / 2n_g \Delta \nu \tag{2.56}$$

Remember the optical frequency has the following relationship with optical wavelength:

$$\nu = c / \lambda \tag{2.57}$$

Differentiating both sides,

$$\Delta \nu = c\Delta\lambda / \lambda^2 \tag{2.58}$$

And substitutes into Eq. 2.57, we got:

$$\Delta z = \lambda^2 / 2n_g \Delta\lambda \tag{2.59}$$

The above Eq. (2.59) describes the relationship between spatial resolution Δz, central wavelength λ, and wavelength tuning range $\Delta\lambda$. Given a fixed central wavelength, the larger wavelength tuning range corresponds to a higher spatial resolution.

Beat Frequency (Sampling Frequency)

By employing the auxiliary interferometer, a constant frequency interval sampling is guaranteed. Suppose the length difference of the two arms in the auxiliary interferometer is l, which corresponds to a time delay of $\tau = l / v_g = n_g l / c$. Also the optical frequency delay between two arms can be found as $\Omega = \tau(d\omega / dt)$.

Converting the units into Hz, the beat frequency is expressed as:

$$\begin{aligned}\upsilon_{beat} &= \Omega / 2\pi = \frac{n_g l}{2\pi c} \bullet \frac{d\omega}{dt} = \frac{n_g l}{2\pi c} \bullet \frac{2\pi d\upsilon}{dt} \cong \frac{n_g l}{c} \bullet \frac{c(\Delta\lambda / \Delta t)}{\lambda^2} \\ &= n_g l \frac{(\Delta\lambda / \Delta t)}{\lambda^2}\end{aligned} \tag{2.60}$$

here $\Delta\lambda / \Delta t$ represents an average wavelength tuning speed. υ_{beat} also represents the data sampling rate. Taking typical values, wavelength tuning range $\Delta\lambda = 40nm$, wavelength tuning time $\Delta t = 1s$, group RI $n_g = 1.45$,a length difference $l = 200m$ and a central wavelength of $\lambda = 1550nm$, one may find $\upsilon_{beat} = 4.83MHz$. This value is of significance as it provides the minimum sampling speed of the DAQ. In fact, υ_{beat} is not constant within the whole tuning process, as a result the sampling rate of DAQ often doubles (~10MHz).

Total Samples

Total samples taken in tuning process are acquired by multiplying υ_{beat} and sampling time $T_{sampling}$, as follows:

$$S_{total} = \upsilon_{beat} \bullet T_{sampling} = n_g l \frac{\Delta\lambda}{\lambda^2} \tag{2.61}$$

Typically, if $T_{sampling} = 1s$, which means TLS sweeps a 40nm wavelength range in 1s, the total samples taken equals 4.83 Mega samples.

When performing an FFT, $T_{sampling}$ reduces to a half due to Nyquist–Shannon sampling theorem:

$$S_{FFT} = \frac{n_g l \Delta\lambda}{2\lambda^2} \tag{2.62}$$

Since the maximum sensing length $l_{FUT} = \frac{1}{4} l_{auxiliary}$:

$$S_{FFT} = \frac{n_g 4 l_{FUT} \Delta\lambda}{2\lambda^2} = \frac{2 n_g l_{FUT} \Delta\lambda}{\lambda^2} \tag{2.63}$$

Therefore, the number of points per meter is simply S_{FFT} / l_{FUT}:

$$S_{P/m} = S_{FFT} / l_{FUT} = \frac{2 n_g \Delta\lambda}{\lambda^2} \tag{2.64}$$

Taking the above parameters, we get $S_{P/m} = 48.3k\, points/m$, thus corresponds to a spatial resolution of $\Delta z = \lambda^2 / 2 n_g \Delta\lambda = 20.7\mu m$, which is exactly the Eq. (2.59).

2.2.4.2 Sensing Resolution vs Spatial Resolution

To define the sensing resolution, one must determine the maximum error in the wavelength shift in performing cross-correlation. The peak wavelength shift by performing a cross-correlation is ideally zero if no environmental disturbance occurs, which indicates an extremely high precision. However, this is not the case in OFDR as only a small portion of spatial points is used to do the cross-correlation. Clearly, a larger number of data will reduce the uncertainty of the wavelength shift but at a cost of lower spatial resolution [35]. Therefore, it is a **trade-off** between the sensing resolution and spatial resolution. Previous work has been done by Xiaozhen Wang. *et*, al. [35], where 100 times OFDR measurements were individually performed without disturbance. Then the cross-correlation was calculated and the wavelength shift was measured as a function of number of data. It is found that the uncertainty is as high as ~17pm at 1mm (80 data points) spatial resolution, while it decreases to ~4pm at 3.85mm (300 data points) spatial resolution. Using the typical temperature response,

the accuracy is found to be $1.7°C$ and $0.4°C$, respectively. For typical OFDR application with 40nm wavelength tuning range, **1cm** spatial resolution commonly corresponds to $\sim 0.1°C$ temperature resolution, which is the best performance in all kinds of distributed fiber sensors.

In summary, the spatial resolution of OFDR system was theoretically analyzed in this chapter, while the sensing resolution is also determined by calculating the uncertainty of the wavelength shift. To guarantee a certain level of sensing resolution, a number of data points have to be taken in cross-correlation which therefore result in a trade-off between spatial resolution and sensing accuracy.

Chapter 3

Extended sensing length of OFDR

3.1 Introduction

In this chapter, several nonlinearity compensation algorithms are proposed and experimentally demonstrated in purpose to extend the sensing length of conventional nonlinear triggered OFDR. In conventional OFDR, an auxiliary interferometer (AI) is employed to trigger data acquisition where an equal frequency interval is guaranteed. However, there are two main drawbacks in using the AI: firstly, the maximum sensing length is limited by the optical path difference (OPD) of AI, which is in fact only a quarter of the OPD of AI in order to satisfy the Nyquist Sampling theorem. Secondly, the OPD of AI must be much shorter than the laser coherent length to generate correct trigger. Even OPD close to coherent length may introduce errors in the triggered signals from the auxiliary interferometer where polarization mode dispersion and phase noise exist. Considering both restrictions, the sensing range of conventional nonlinear triggered OFDR is less than one quarter the coherent length of TLS. In fact, the commercial OFDR system in market has a sensing length of only 70m [38].

As discussed above, the sensing length cannot exceed the coherence length of TLS. However, it could be significantly extended (close to coherence length of TLS) if the auxiliary interferometer is not employed, which requires some other techniques to

suppress the tuning nonlinearities. Several approaches have been proposed regarding this issue: Firstly, one could use laser sources of linear frequency tuning within a microwave frequency domain over a small tuning range by an electrical optical modulator [51], however, small tuning range corresponds to poor sensing accuracy, which limits its usage. Another method is to compensate the tuning nonlinearity of the TLS frequency scanning afterwards, in other words to resample signals from OFDR with an equal frequency interval where the optical frequency can be extracted from the auxiliary interferometer [34, 50-60]. This is a promising approach to extend the sensing length to as long as laser coherent length but previous works only focus on fault locating rather than sensing.

In this chapter, we adopt 3 different data processing approaches, including non-uniform fast Fourier transform (NU-FFT), Deskew filter and cubic spline interpolation, to resample the data from OFDR. Resampling principles, performances are discussed for each approach. The result indicates that, one of those algorithms -- cubic spline interpolation resamples data with high accuracy which is capable for distributed temperature and strain sensing.

3.2 Frequency Tuning Nonlinearity Compensation by Using Non-Uniform FFT (NUFFT)

I came to a variety of approaches in order to compensate the frequency tuning nonlinearity in OFDR system where the Non-Uniform Fast Fourier Transform

(NU-FFT) is the first trial I made in order to realize data resampling. NU-FFT [57, 61, 62] is a resampling scheme that is well accepted for non-equal spaced sampling in frequency domain, which has been applied in many applications like Magnetic Resonance Imaging (MRI) [62], Optical Coherence Tomography [55, 63, 64], and other applications.

3.2.1 Theory of NU-FFT

The basic principle of frequency tuning nonlinearity compensation using NU-FFT is to resample the beat signal in the main interferometer where the nonlinear instantaneous frequency was subtracted from an auxiliary interferometer. The auxiliary interferometer consists of two couplers, where two sections of fibers are connected with an OPD. Suppose the group delay difference of the two arms is τ, the interference signal can be expressed as [54],

$$I(t) = U_0 \cos\left(2\pi\tau v(t)\right) \tag{3.1}$$

Where U_0 is the amplitude of the beat signal, and v(t) is the instantaneous optical frequency of the tunable laser source (TLS), the DC term in I(t) is automatically removed as the photo detector is AC coupled. To obtain the instantaneous optical frequency v(t), a Hilbert transform can be applied to the interference signal, where an $\pi/2$ is added on phase term of I(t), and we can get,

$$I_H(t) = \mathrm{H}\{I(t)\} = U_0 \cos\left(2\pi\tau v(t) + \pi/2\right) = U_0 \sin\left(2\pi\tau v(t)\right) \tag{3.2}$$

Finally, the instantaneous optical frequency is recovered as follows,

$$v(t) = \tan^{-1}\left(I_H(t)/I(t)\right)\Big/\left(2\pi\tau\right) \tag{3.3}$$

Since the recovered v(t) is within the interval (-1/(4τ), 1/(4τ)), an unwrapping process is needed to remove the discontinuities in v(t) and retrieve the true instantaneous optical frequency values which are sampled at equal time intervals between data points.

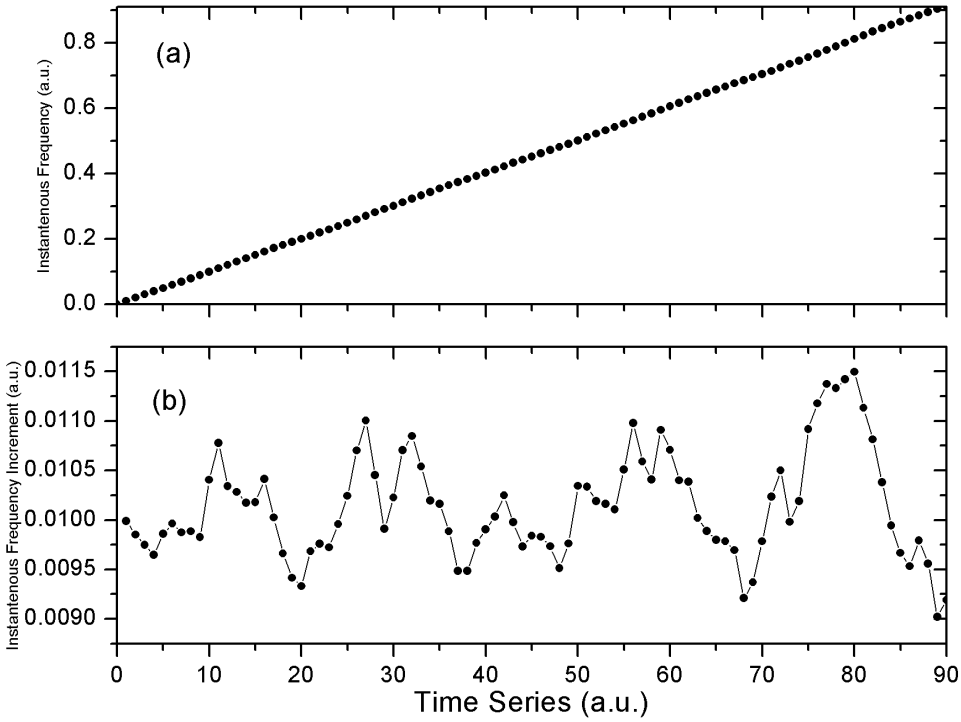

Fig. 3.1 Real data of recovered (a) instantaneous optical frequency and (b) instantaneous optical frequency increment

Fig. 3.1 is the result of the recovered (a) instantaneous optical frequency and (b) instantaneous optical frequency differentiation; at first sight it is found that in (a) that the optical frequency seems linear with respect to time evolution. However, a more obvious proof can be found if we differentiate the instant optical frequency with time, which is shown in (b), where the increment of frequency is highly unequal. This

nonlinearity leads to tremendous deterioration of the spatial resolution of OTDR-like trace, preventing further sensing application, which requires highly accurate spatial Rayleigh backscattering profile.

The instantaneous optical frequency is then normalized for the second step resampling algorithm. In main interferometer, the frequency-modulated continuous wave (FMCW) beat signal is formed by the interference of the reference arm and the backscattered arm at different locations along the FUT. As shown in Fig. 3.1, the beat signal is sampled at an equal time interval and due to the nonlinearity in frequency tuning, the frequency is not sampled with equal interval.

A NU-FFT is then applied to resample the non-equal tuning frequency, the normalized frequency works as an independent variable which the beat signal in main interferometer is corresponding to. The NU-FFT process is started by convoluting the non-equal frequency with a kernel Gaussian function $\varpi(\nu_n)$, which can be expressed as below,

$$x(\nu_k) = \sum_{n=0}^{N-1} x(\nu_n)\varpi(\nu_n - \frac{k}{K}), k \in [0, K-1] \quad (3.4)$$

Where $\varpi(\nu_n)$ is an optimized Gaussian function [57]: $\varpi(\nu_n) = \exp(-\nu_n^2 / 4\tau)$, $\tau = \pi N_{sp} / [2N^2\alpha(\alpha - 0.5)]$ and N_{sp} is the number of points included for calculation, α the oversampling factor, N the total sampling points [57]. In theory, the Gaussian function $\varpi(\nu_n)$ has an infinite range which requires huge calculation loads; therefore, the Gaussian function is limited in a length to reduce the computation time. The $x(\nu_k)$ is the summation of the values that satisfies $|\nu_n - k/K| \leq N_{sp}/2K$, where ν_n is obtained by the auxiliary interferometer.

The $x(\nu_k)$ is now an uniformly sampled frequency, which is then converted to OTDR-like trace, $X_G(z_n)$, after a regular FFT. Finally, $X_G(z_n)$ is de-convoluted by the following approximation

$$X(z_n) \approx X_{app}(z_n) = \frac{X_G(z_n)}{W(z_n)} \tag{3.5}$$

Where $W(z_n)$ is the FFT of Gaussian kernel $\varpi(\nu_n)$.

3.2.2 Experimental Result on Simulation data

The first trial I made was based on a simulated data, in order to verify the correctness of this approach.

To generate a simulated data, the FUT is supposed to have one dominant Fresnel reflection peak at a certain frequency (position), then some noise is added to the phase term in $I(t)$ so that $I(t) = U_0 \cos\left(2\pi\tau\nu_{linear}(t) + A_{\text{mod}} \cos(\varpi_{\text{mod}} t)\right)$ which will result in frequency expanding. In this trial, a 100k points data set is generated using a self-made program.

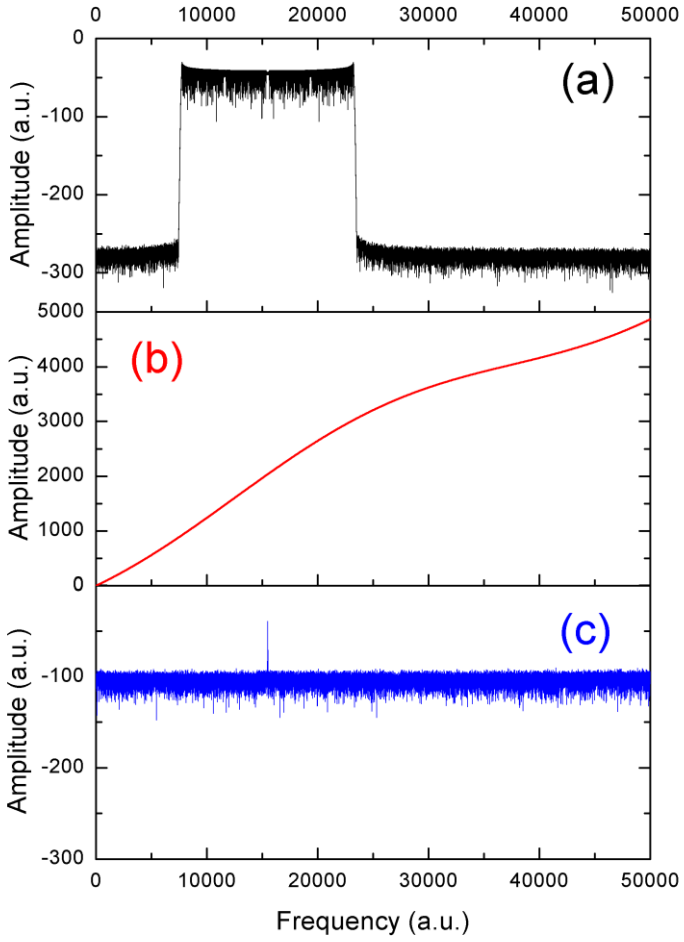

Fig. 3.2 OTDR-like trace (a) before NU-FFT (b) nonlinear instantaneous phase and (c) after NU-FFT

Fig. 3.2 (a) shows the OTDR-like trace, due to the frequency broadening effect, the single Fresnel reflection expands to a length of reflections. Fig. 3.2 (b) shows the phase evolution of the TLS, which is obviously not linear. This degraded OTDR-like trace is then resampled by use of NU-FFT, which is shown in Fig. 3.2 (c).

A significant improvement in spatial resolution can be easily found by comparing Fig. 3.2 (a) and Fig. 3.2 (c). In Fig.3.2 (c), the broadened frequency component is reduced to one dominant frequency, which provides similar result to that with no phase noise

which verifies the correctness of this method. To make a more detailed comparison, Fig. 3.2 (a) and Fig. 3.2 (c) are plotted with the same log scaling factors. We found that the noise floor after the NU-FFT is about -100dB, while in Fig. 3.2 (a), the noise floor of the deteriorated frequency data is -300dB which is much lower than the compensated one. The increasing noise floor might decrease the Signal to Noise Ratio (SNR), which is not beneficial to experiments. However, the compensated signal keeps fairly high SNR which in my point of view might not affect the result.

3.2.3 Experimental Result on Real data

As NU-FFT is capable of resampling the simulated data, the next step is to examine its actual performance on real data.

When it comes to real data, one thing that should be addressed is to guarantee that the nonlinear phase is recovered correctly. In simulation data, the phase was intentionally modified by a nonlinear term with slowly varying frequency and amplitude, which makes the recovery of the phase easy. However, this is not the case in real data, as our initial purpose is to make long range distributed sensing, which theoretically requires large frequency sweeping range in order to achieve high temperature or strain sensitivity. Given the maximum sampling rate and buffer of the data acquisition card (DAQ), large frequency sweeping range requires fairly high frequency tuning speed, which means only few points is within a 2π period in phase. In discrete signal processing, the unwrapping phase progress commonly requires enough points within a

beat length to track and repair the discontinuities in the recovered phase. In my trials, the wavelength sweeping speed is finally 5.9nm per second which commonly recovers the phase correctly. The detailed calculations about the relation of wavelength sweeping speed and sampling rate of the DAQ will be discussed in the Spline Interpolation section.

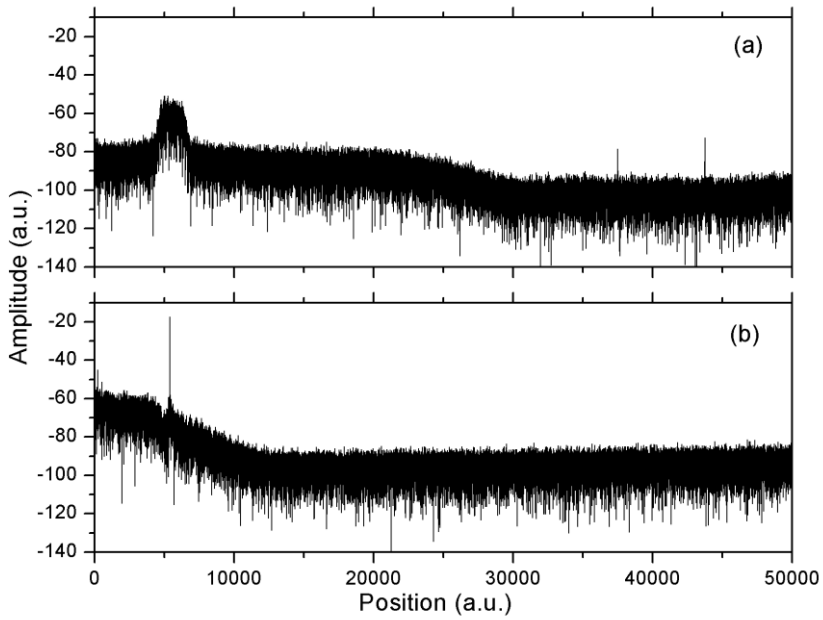

Fig. 3.3 Real data OTDR-like trace (a) before NU-FFT and (b) after NU-FFT

Fig. 3.3 shows (a) the original OTDR-like trace and (b) the recovered OTDR-like trace using NU-FFT. TLS sweeps from 1550nm to 1556nm with 5.9nm/s sweeping speed, a 10M points per second sampling rate and 1 second data acquisition. To speed up the calculation, only 100K points are used in resampling the data.

In Fig. 3.3 (a), one peak could be easily found with huge frequency broadening, while in Fig. 3.3 (b) it is recovered to be very sharp and shows a very high spatial resolution. However, a significant drawback can be found in Fig. 3.3 (b) that the shape of the

recovered signal is clearly a Gaussian instead of a commonly seen OTDR-like trace. The reason shall be discussed in following section.

3.2.4 Limitations of NU-FFT

In Chap. 3.2.3, it is found that the recovered OTDR-like trace has a Gaussian shape which tremendously reduces the sensing range. The reason to this drawback could be explained as follows: the NU-FFT is actually an approach where the original raw data $x(\nu_n)$ convolutes with the Gaussian kernel function $\varpi(\nu_n)$, according to convolution:

$$F(x(\nu_n) * \varpi(\nu_n)) = k \bullet X(z_n) \bullet W(z_n) \tag{3.6}$$

Where k is a constant that depends on the specific normalization of the Fourier transform, $X(z_n)$ is the FFT of $x(\nu_n)$, and $W(z_n)$ the FFT of $\varpi(\nu_n)$, which result in a Gaussian envelope in frequency spectrum and blurs the original flat OTDR-like trace. By using the de-convolution approximation, this envelope can be mitigated to some degree, however, at far frequency both the convoluted term $X_G(z_n)$ and FFT of Gaussian kernel $W(z_n)$ are almost zero, as seen in Fig. 3.3 (b), these two small decimals division would result in large error that in fact even larger than error induced by nonlinearity itself, which limits the available length of NU-FFT approach. By changing Gaussian kernel parameters like the over-sampling factor, the Gaussian kernel leads to more broadening, which means longer sensing length can be achieved, however, after all this NU-FFT cannot guarantee availability within the

whole range of the OTDR-like trace.

To make a summary, the NU-FFT approach to compensate for the nonlinearity in OFDR is theoretically proven using a simulated broadened Fresnel reflection point and experimentally demonstrated. The NU-FFT compensates the simulated data with very good accuracy, however, when it comes to real data, NU-FFT is found to possess a Gaussian envelope which blurs the OTDR-like trace that limits the total sensing distance. As our final goal is to achieve long distance and high spatial resolution OFDR sensing, the NU-FFT cannot satisfy all the requirements.

3.3 Frequency Tuning Nonlinearity Compensation by Using Deskew Filter

As the NU-FFT approach cannot maintain OTDR-like trace within the whole sensing length, one must find a new approach, which compensates the frequency tuning nonlinearity without inducing new difficulties.

Considering the principles of OFDR is similar to that of frequency modulated radar in radio frequency region, where some useful works have been done to reduce the tuning nonlinearity in microwave band, my idea came to that maybe some algorithms could be borrowed from radio frequency signal processing field. Luckily, some pioneering works have been done, where Deskew filter is employed to reduce the degradation of optical frequency tuning nonlinearity of the TLS in a long range [58]. The Deskew filter is also known as Residual Video Phase (RVP) filter which originated from

Frequency Modulated Continuous Wave Synthetic Aperture Radar (FMCW SAR) where frequency tuning or chirping nonlinearity also exists [65-67]. In theory, this approach could eliminate all the tuning nonlinearity resulting from TLS if the nonlinear phase could be predicted accurately. In [58] Ding proposed a 80km distributed OFDR configuration with 20cm and 1.6m spatial resolution at distances of 10km and 80km, thus might become a powerful tool for long range distributed temperature and strain sensing based on OFDR, where a large frequency tuning range is required.

3.3.1 Theory of Deskew filter

As explained in previous chapter, the main interferometer in OFDR consists of two arms, one named $E_s(t)$ undergoes the fiber under test (FUT) while the other one follows a reference path known as $E_r(t)$.

For TLS with a linear optical frequency tuning speed γ, the electrical field $E_r(t)$ could be written as,

$$E_r(t) = E_0 \exp\{j[2\pi f_0 t + \pi\gamma t^2 + 2\pi e(t)]\} \tag{3.7}$$

Where f_0 is the optical frequency, $e(t)$ the nonlinear phase term of TLS.

Assuming the reflection reflectivity at certain time delay τ is $r(\tau)$ and the fiber attenuation coefficient is α, the signal $E_s(t)$ could be written as,

$$E_s(t) = \sqrt{R(\tau)}E_0 \exp\{j[2\pi f_0(t-\tau) + \pi\gamma(t-\tau)^2 + 2\pi e(t-\tau)]\} \tag{3.8}$$

Then at the coupler an AC coupled beat signal $I(t)$ interfered between local

reference term $E_r(t)$ and signal term $E_s(t)$ could be written as,

$$I(t) = 2\sqrt{R(\tau)}E_0^2 \cos\{2\pi[f_0\tau + f_b t + \frac{1}{2}\gamma\tau^2 + e(t) - e(t-\tau)]\} \quad (3.9)$$

where f_b is the beat frequency and $f_b = \gamma\tau$ corresponds to different locations in the spatial domain. The last two terms $e(t) - e(t-\tau)$ represent tuning nonlinearity induced by TLS which degrades the spatial resolution and is to be eliminated.

A complex exponential expression is provided by doing Hilbert transform to the above equation that can be expressed as,

$$I(t) = 2\sqrt{R(\tau)}E_0^2 \exp[j2\pi(f_0\tau + f_b t + \frac{1}{2}\gamma\tau^2)]S_e(t)S_e^*(t-\tau) \quad (3.10)$$

Where $S_e(t) = \exp[j2\pi e(t)]$ and $S_e^*(t-\tau) = \exp[-j2\pi e(t-\tau)]$.

To eliminate the nonlinear term $e(t) - e(t-\tau)$, a three step procedure can be done as follows:

1. $$I_1(t) = I(t)S_e^*(t) = 2\sqrt{R(\tau)}E_0^2 \exp[j2\pi(f_0\tau + f_b t + \frac{1}{2}\gamma\tau^2)]S_e^*(t-\tau) \quad (3.11)$$

   Where $S_e^*(t)$ is a complex conjugate of $S_e(t)$ and is assumed to be pre-known, the detailed estimation of $S_e^*(t)$ will be discussed in the next section.

2. $$I_2(t) = F^{-1}\{F\{I_1(t)\}\exp(j\pi f^2/\gamma)\} \quad (3.12)$$

   Where F^{-1} and F denotes inverse Fourier transform and Fourier transform, respectively. The last term $\exp(j\pi f^2/\gamma)$ is called Deskew filter which removes the signal's dependence on distance.

   By solving this equation, we get,

   $$I_2(t) = 2\sqrt{R(\tau)}E_0^2 \exp[j2\pi(f_0\tau + f_b t)]F^{-1}\{S_e^*(-f)\exp(j\pi f^2/\gamma)\} \quad (3.13)$$

   Which removes the distance dependence, and the last Fourier term can be solved

as follows.

3. $$S(t) = F^{-1}\{F\{S_e^*(t)\}\exp(j\pi f^2/\gamma)\} = F^{-1}\{S_e^*(-f)\exp(j\pi f^2/\gamma)\} \quad (3.14)$$

Therefore,

$$I_3(t) = I_2(t) \bullet S^*(t) = 2\sqrt{R(\tau)}E_0^2 \exp[j2\pi(f_0\tau + f_b t)] \quad (3.15)$$

We may find here the tuning nonlinearity is perfectly removed by adopting above algorithm provided the nonlinear term $e(t)$ is known. However, in reality one must find ways to estimate $e(t)$. By employing the auxiliary interferometer which has been previously described in NU-FFT section, one may find that the beat signal can be expressed as follows,

$$I_{ref}(t) = \cos\{2\pi[f_0\tau_{ref} + \gamma\tau_{ref}t + \frac{1}{2}\gamma\tau_{ref}^2 + e(t) - e(t-\tau_{ref})]\} \quad (3.16)$$

The difference between Eq. (3.16) and Eq. (3.1) in NU-FFT is that $I_{ref}(t)$ in NU-FFT is AC-coupled, where the DC term $f_0\tau_{ref} + \frac{1}{2}\gamma\tau_{ref}^2$ is automatically removed and the nonlinearity term $e(t) - e(t-\tau_{ref})$ is included in instantaneous optical frequency $\tau_{ref}v(t)$. The next step is to estimate the nonlinear phase term where a Hilbert transform is applied and the total phase term is subtracted. By linear fitting the phase the nonlinear term $e(t) - e(t-\tau_{ref})$ can be also separated. For a small OPD corresponding to a time delay of τ_{ref}, the nonlinear phase $e(t)$ can be estimated using Taylor series as [66],

$$e(t) - e(t-\tau_{ref}) \approx e(t)'\tau_{ref} \quad (3.17)$$

Where $e(t)'$ corresponding to the derivative of $e(t)$, finally the estimation of $e(t)$ is obtained as follows,

$$e(t) = \int^{t} \frac{e(\mu) - e(\mu - \tau_{ref})}{\tau_{ref}} d\mu \tag{3.18}$$

3.3.2 Experiment Result on Simulation data

Similar to NU-FFT approach, the algorithm is firstly verified by using a simulated data. The simulation consists of two parts: one is the simulation of the nonlinearity and the other one is the verification of the Deskew filter.

For nonlinearity term $e(t) - e(t - \tau_{ref})$, one must generate nonlinearity with exactly the same form of nonlinearity with all other parameters close or similar to real OFDR configurations. During my simulations, I chose the nonlinear term $e(t) = A\cos(\omega t)$, where A denotes the nonlinear term amplitude, ω denotes the nonlinear term frequency, and $e(t - \tau_{ref}) = A\cos(\varpi(t - \tau_{ref}))$ is a delayed version of the nonlinear term. Fig. 3.4 shows the program of function generator written in LabView.

For other parameters required in this function generator, I chose sweeping speed=2nm/s, $\gamma = 1.25 \times 10^{11} Hz / s$ is the frequency tuning speed at 1550nm. τ is the delay time corresponding to a particular location.

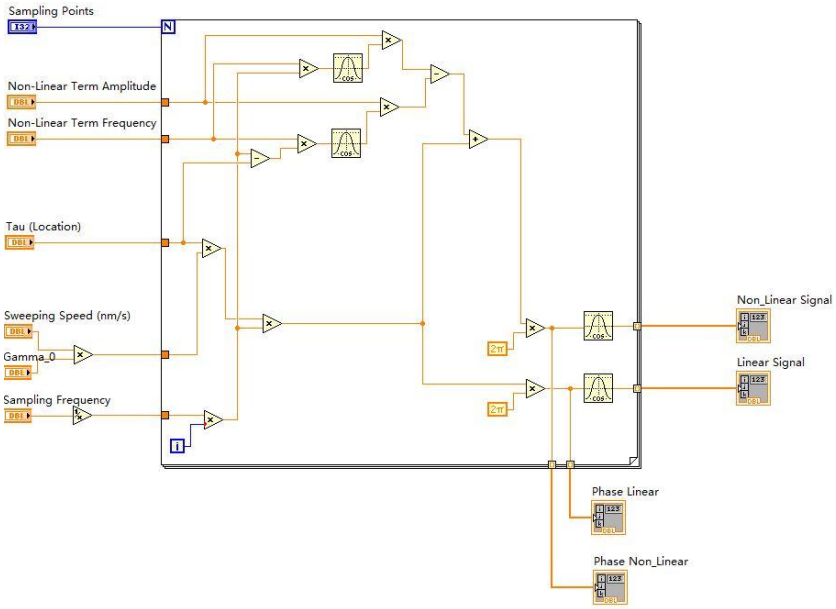

Fig. 3.4 Function Generator written in LabView

The next step is to use this function generator to generate both signals in main interferometer and in auxiliary interferometer and based on which one can verify the correctness of Deskew filter.

Fig. 3.5 provides the simulated result of the Deskew filter. Fig. 3.5 (a) shows the OTDR-like trace with no nonlinearity, in which a perfect single Fresnel reflection is shown. Fig. 3.5 (b) shows the OTDR-like trace with nonlinearity, where frequency broadening is spotted around the single Fresnel reflection point. Fig. 3.5 (c) shows the OTDR-like trace with nonlinearity and compensated by Deskew filter. Fig. 3.5 (c) shows that the frequency broadening is tremendously reduced in comparison with Fig. 3.5 (b), besides, the noise floor is also reduced for more than 40 dB and is almost same to that in Fig. 3.5 (a). By compensating the nonlinearity of a simulated data, a correctness of the Deskew filter is verified which is then used in real data processing. Before ending this section, the program of Deskew filter is also provided as part of

my thesis contents in Fig. 3.6.

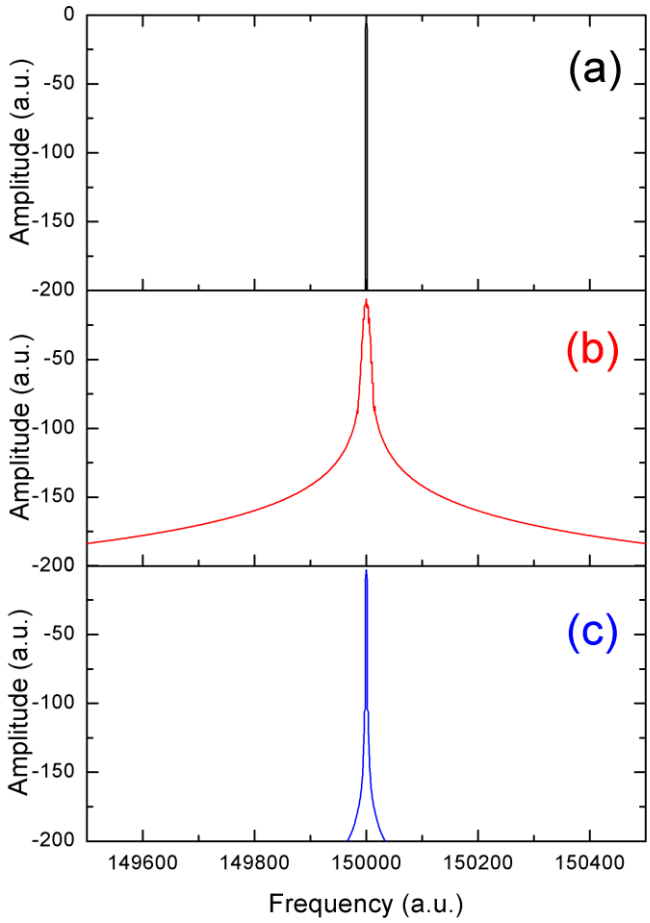

Fig. 3.5 Experimental result on simulated data. (a) simulated one Fresnel reflection point with no nonlinear term (b) simulated one Fresnel reflection point with nonlinear term (c) simulated one Fresnel reflection point compensated by Deskew filter

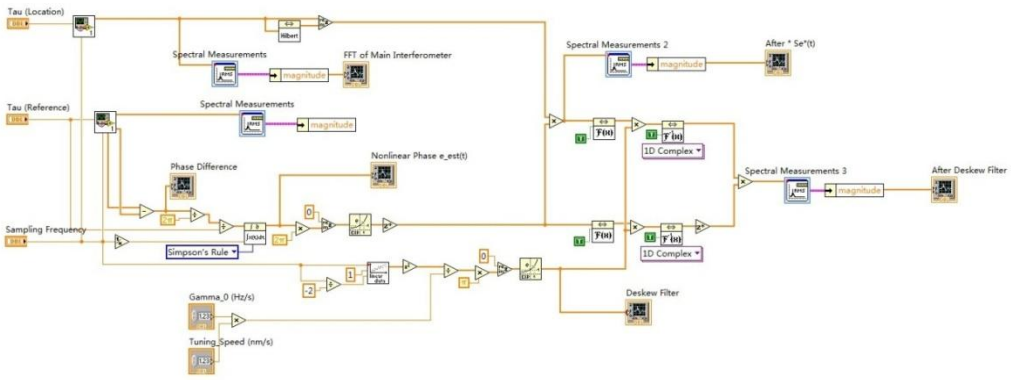

Fig. 3.6 Deskew filter to compensate the nonlinearity in simulated data written in

3.3.3 Experiments based on Real data

Similarly, as the Deskew filter algorthm functions well with the simulated data, the next step is to examine its actual performance on real data.

To make a more recognizable comparison, the sweeping parameters are identical to that in NU-FFT algorithm: One Fresnel reflection is intentionally made and TLS sweeps from 1550nm to 1556nm with 5.9nm/s sweeping speed, a 10M points per second sampling rate with 1 second data acquisition and a 100K points are used in resampling the data. Fig. 3.7 is the program I made for the real data processing, where a nonlinear phase prediction subroutine is written.

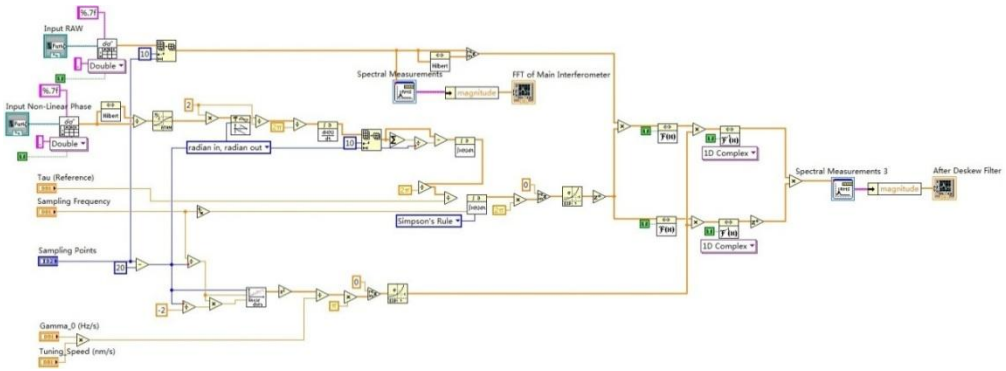

Fig. 3.7 Deskew filter to compensate the nonlinearity in real data with a nonlinear phase prediction subroutine

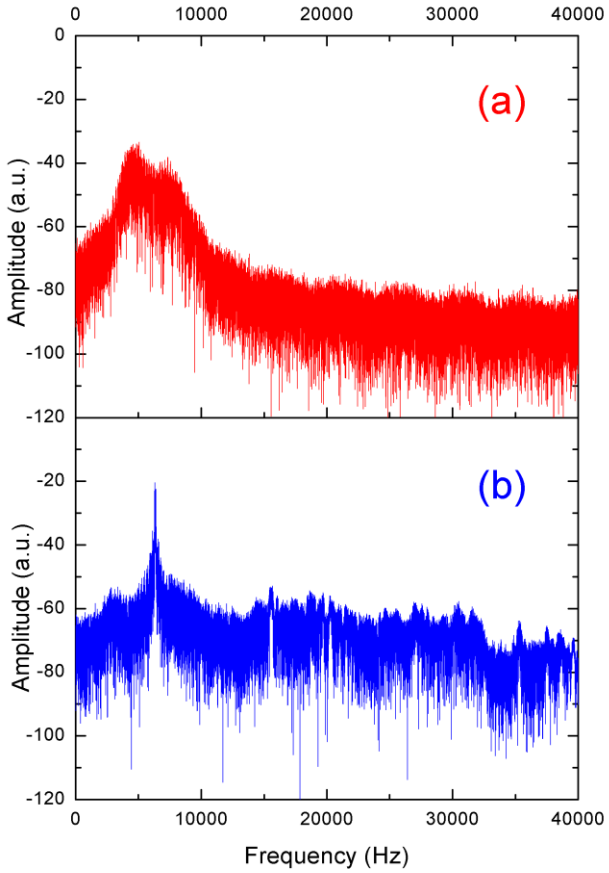

Fig. 3.8 Real data OTDR-like trace (a) before Deskew filter and (b) after Deskew filter

Fig. 3.8 shows (a) the original OTDR-like trace and (b) the recovered OTDR-like trace using Deskew filter. In Fig. 3.8 (a), due to the frequency tuning nonlinearity, the Fresnel reflection peak is broadening while in Fig. 3.8 (b) it is compensated by Deskew filter, which provides a very sharp peak. Comparing to NU-FFT algorithm, one may easily find that there is no Gaussian envelope over the entire frequency range, which shows some better potential over the NU-FFT algorithm.

3.3.4 Limitations on Physics

Although the Deskew filter is effective in recovering the Fresnel reflection, we may find that the wavelength tuning range in the previous section is only 59pm (or equivalently 7.5 GHz), which is a fairly small tuning range. However, if we increase the tuning range, two major problems came out which had not been revealed in reference [58]. The first problem is that, as Deskew filter originated from Radar, where EM-field propagates in air,and where no or only little group velocity dispersion exists, therefore, the frequency tuning speed γ can be assumed to be a constant over the entire frequency tuning range. However, in order to achieve high temperature and strain sensitivity, the frequency tuning range has to be large as the sensitivity is proportional to the frequency tuning range, as a result, the frequency tuning speed γ is not a constant anymore for 5.9nm sweeping range, which means $\gamma = \gamma(f)$ and the Deskew filter term $\exp(j\pi f^2/\gamma(f))$ cannot be perfectly generated. The second problem is that, in the phase term $2\pi[f_0\tau_{ref} + \gamma\tau_{ref}t + \frac{1}{2}\gamma\tau_{ref}^2 + e(t) - e(t-\tau_{ref})]$, the linear term $f_0\tau_{ref} + \gamma(f)\tau_{ref}t + \frac{1}{2}\gamma(f)\tau_{ref}^2$ is frequency dependent and cannot be fitted using a linear fitting, which leads to difficulties to extract the nonlinear term $e(t) - e(t-\tau_{ref})$ and lastly leads to errors in recovering the nonlinearity. During my tests, the Deskew filter only works for a fairly small frequency tuning range (~ GHz). For large tuning range (5.9nm or equivalently ~750GHz), the Deskew filter cannot recover the phase correctly.

To make a summary, the Deskew filter is theoretically deduced and examined using

both simulated data and real data. For a simulated Fresnel reflection point, the Deskew filter compensates the nonlinearity effectively as nonlinear phase was predicted perfectly, a more than 10 times spatial resolution was found. However, when it comes to real data, as the frequency tuning speed $\gamma(f)$ is a function of optical frequency, the larger the frequency tuning range, the more $\gamma(f)$ changes and leads to poorer compensation. Therefore, the Deskew filter only works for a small frequency tuning range and cannot be adapted in temperature or strain sensing which requires a large frequency tuning range.

3.4 Cubic Spline Interpolation

The third approach we proposed to treat tuning nonlinearities of OFDR is also a resampling scheme. There are limits of previous approaches: NU-FFT is found to be only working at short distance within the whole sensing range, and Deskew filter is only capable for a small wavelength tuning range. Considering all those drawbacks, the cubic spline interpolation approach is demonstrated to be able to function within a large wavelength tuning range as well as to maintain high resampling accuracy.

3.4.1 Theory of Cubic spline interpolation

The cubic spline interpolation is a form of interpolation where the interpolant is a special type of piecewise polynomial named a spline. Spline interpolation is favorable

over other polynomial interpolation because the interpolation error can be made trivial even when low degree polynomials are employed for the spline. Another advantage is that spline interpolation avoids the problem of Runge's phenomenon, which occurs when employing higher order polynomial interpolation [68].

Now suppose a polynomial q(x) has the following values [69, 70]:

$$\begin{aligned} q(x_1) &= y_1 \\ q(x_2) &= y_2 \\ q'(x_1) &= k_1 \\ q'(x_2) &= k_2 \end{aligned} \tag{3.19}$$

A symmetrical form can be written using above parameters:

$$q = (1-t)y_1 + ty_2 + t(1-t)(a(1-t)+bt) \tag{3.20}$$

where $t = \dfrac{x - x_1}{x_2 - x_1}$ and,

$$\begin{aligned} a &= k_1(x_2 - x_1) - (y_2 - y_1) \\ b &= -k_2(x_2 - x_1) + (y_2 - y_1) \end{aligned} \tag{3.21}$$

As $q' = dq/dx = \dfrac{dq}{dt}\bullet\dfrac{dt}{dx} = \dfrac{dq}{dt}\bullet\dfrac{1}{x_2 - x_1}$, one may get first order derivative,

$$q' = \frac{y_2 - y_1}{x_2 - x_1} + (1-2t)\frac{a(1-t)+bt}{x_2 - x_1} + t(1-t)\frac{b-a}{x_2 - x_1} \tag{3.22}$$

And second order derivative,

$$q'' = 2\frac{b - 2a + (a-b)3t}{(x_2 - x_1)^2} \tag{3.23}$$

Setting $x = x_1$ and $x = x_2$ respectively in Eq. (3.22), one may verify the first order derivatives $q'(x_1) = k_1$ and $q'(x_2) = k_2$ are automatically satisfied. The second order derivatives are as follows:

$$q''(x_1) = 2\frac{b-2a}{(x_2-x_1)^2}$$
$$q''(x_2) = 2\frac{a-2b}{(x_2-x_1)^2} \tag{3.24}$$

Above discussion is based on two points interpolation, if a data set with n points is to be interpolated, the interpolated curve has the form of:

$$q_i = (1-t)y_{i-1} + ty_i + t(1-t)(a_i(1-t) + b_i t) \tag{3.25}$$

where $i = 1, 2, ..., n$ and $t = \frac{x - x_{i-1}}{x_i - x_{i-1}}$ are n polynomials interpolating y in the interval $x_{i-1} \le x \le x_i$ for $i = 1, 2, ..., n$ such that the first order derivative $q'_i(x_i) = q'_{i+1}(x_i)$ at each point. Those n polynomials define a differentiable curve within $x_0 \le x \le x_n$.

Similarly, we have definition for a and b:

$$a_i = k_{i-1}(x_i - x_{i-1}) - (y_i - y_{i-1})$$
$$b_i = -k_i(x_i - x_{i-1}) + (y_i - y_{i-1}) \tag{3.26}$$

And

$$k_0 = q'_1(x_0)$$
$$k_i = q'_i(x_i) = q'_{i+1}(x_i), \quad i = 1, 2, ..., n-1 \tag{3.27}$$
$$k_n = q'_n(x_n)$$

The above equations give a smooth curve with continuous first order derivative at each knot. A more smooth curve with continuous second order derivative can be obtained if the sequence $k_1, k_2, ..., k_n$ satisfies $q''_i(x_i) = q''_{i+1}(x_i)$.

From Eq. (3.24), (3.25), (3.26), (3.27) we may find this is the case if and only if

$$\frac{k_{i-1}}{x_i - x_{i-1}} + \left(\frac{1}{x_i - x_{i-1}} + \frac{1}{x_{i+1} - x_i}\right)2k_i + \frac{k_{i+1}}{x_{i+1} - x_i} = 3\left(\frac{y_i - y_{i-1}}{(x_i - x_{i-1})^2} + \frac{y_{i+1} - y_i}{(x_{i+1} - x_i)^2}\right) \tag{3.28}$$

For $i = 1, 2, ..., n$, the relations above are n-1 linear equations for n+1 values

$k_1, k_2, ..., k_{n-1}$.

At the boundary where $x = x_0$ and $x = x_n$, the second order derivatives are intentionally made zero, in which way k_0 and k_n are determined:

$$q''_1(x_0) = 2\frac{3(y_1 - y_0) - (k_1 + 2k_0)(x_1 - x_0)}{(x_1 - x_0)^2} = 0,$$
$$q''_n(x_n) = 2\frac{3(y_n - y_{n-1}) - (2k_n + k_{n-1})(x_n - x_{n-1})}{(x_n - x_{n-1})^2} = 0, \quad (3.29)$$

Finally, Eq. (3.28) together with Eq. (3.29) constitute n+1 linear equations that interpolate n curves with continuous first order derivative and second order derivative. This interpolation scheme is named cubic spline interpolation as it is a third order polynomial fitting.

3.4.2 Applying cubic spline interpolation in data resampling

Similar to NU-FFT and deskew filter, cubic spline interpolation requires non-equal spaced instantaneous optical frequency, which can be subtracted from auxiliary interferometer. The beat signal generated from the auxiliary interferometer can be expressed as [57],

$$I(t) = U_0 \cos\left(2\pi\tau v(t)\right) \quad (3.30)$$

where U_0 is the amplitude of the beat signal, τ is the group delay difference between the two arms of the MZI, and *v(t)* is the instantaneous optical frequency of the TLS which can be recovered by use of the Hilbert transform,

$$v(t) = \tan^{-1}\left(I_H(t)/I(t)\right)/\left(2\pi\tau\right) \quad (3.31)$$

Where

$$I_{\mathrm{H}}(t)=\mathrm{H}\{I(t)\}=U_0\sin\left(2\pi\tau v(t)\right) \tag{3.32}$$

Since the recovered v(t) is within the interval (-1/(4τ), 1/(4τ)), an unwrapping process is needed to remove the discontinuities in v(t) and retrieve the true instantaneous optical frequency values.

Then, the instantaneous optical frequency is normalized and regarded as $x_0, x_1, ..., x_n$ in above equations, while the data from the main interferometer is corresponding to $y_0, y_1, ..., y_n$. By doing so, the beat signal from OFDR is resampled to acquire an interference fringe with equal frequency spacing by using the cubic spline interpolation algorithm.

A schematic illustration of cubic spline interpolation with uneven sampling intervals is given as follows:

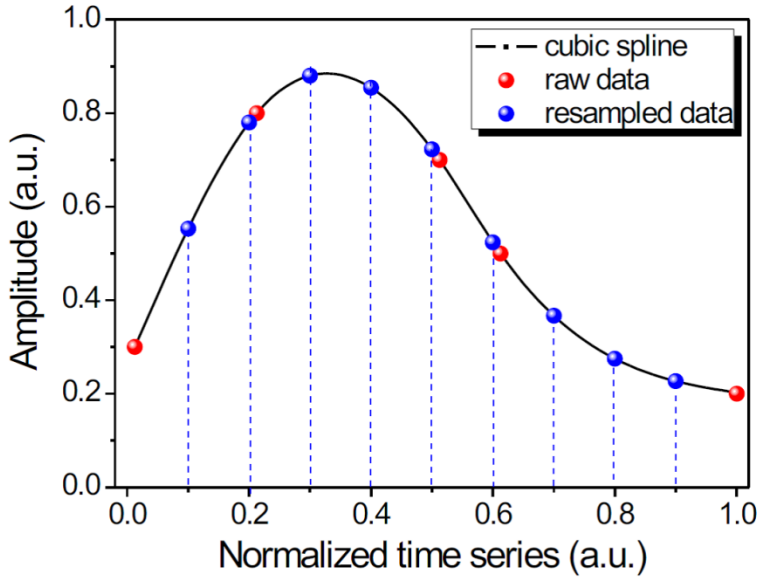

Fig. 3.9 Illustration of cubic spline interpolation with uneven sampling intervals

The red dots in Fig. 3.9 represent a non-equal spaced data (raw data), while the blue dots represent resampled data after applying cubic spline interpolation. From this

illustration, an apparent advantage of cubic spline interpolation is that it creates a smooth interpolated curve with relatively small error. Besides, the interpolation is much easier to evaluate which provides optimal interpolation accuracy with fast interpolation time.

3.4.3 Experimental details

Fig. 3.10 shows the experimental setup designed for distributed temperature and strain measurements over a long distance. The configuration of the OFDR system consists of a TLS (Newfocus TLB6600), a main interferometer with a polarization beam splitter (PBS) based polarization diversity receiver, an auxiliary interferometer with 100-meter OPD to measure instantaneous optical frequency, photo detectors (PDs) and a data acquisition card (DAQ, NI PCI-6115, maximum of 10 million samples per channel at 12 bit accuracy). One polarization controller (PC) within the main interferometer and another PC in front of the FUT are adopted to adjust light polarization states. An interference signal is from PBS to obtain a polarization-independent signal by calculating a vector sum of p- and s-components of the detected signals. The complex Fourier transform is carried out to convert the wavelength-domain signal into an optical time-domain reflectometry (OTDR) like trace along the FUT length. An Intel i7 3612qm mobile processor is employed for cubic spline interpolation and cross-correlation.

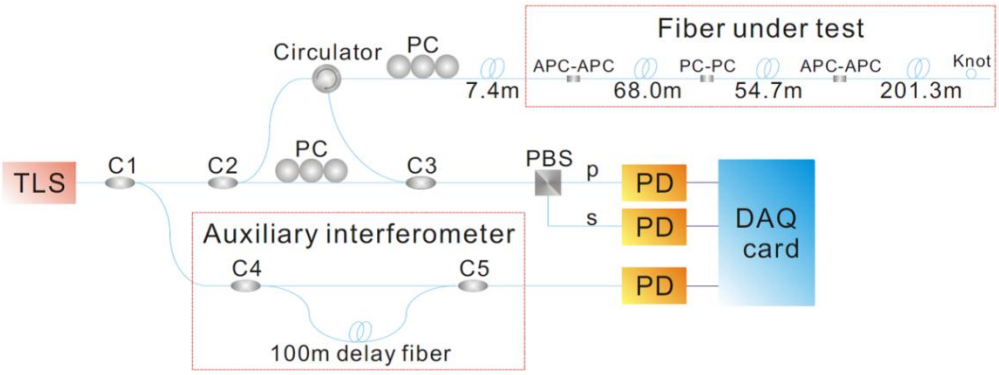

Fig. 3.10 The configuration of the OFDR system for long range distributed temperature and strain measurement. TLS: tunable laser source; C1: 1:99 optical coupler; C2~C5: 50:50 optical coupler; PC: polarization controller; PBS: polarization beam splitter

The FUT consists of three sections of different lengths of 68.0 m, 54.7 m and 201.3 m concatenated by a pair of angled physical contact (FC-APC) connectors, a pair of physical contact (FC-PC) connectors, and another APC-APC connection, respectively. The fiber length before the first APC-APC connection is 7.4 m. A fiber knot with a small bending radius is deliberately induced at the end of the FUT to reduce the Fresnel reflection. The TLS sweeps from 1550 nm to 1556 nm. The DAQ card operates at an average sampling rate of 10 MS/s with a total 9.9 million sampling points. Different temperature and axial strain were applied to the FUT at different positions to calibrate the thermally and mechanically induced wavelength shift. The surrounding temperature was changed by using an oven at two different locations of 10.0 m extending over 1.8 m and 84.5 m over 40.0 m, while the temperature of the other part of the FUT is maintained at room temperature. The axial strain was changed by using translation stages at two locations of 8.5 m and 75.5 m with the same length of 0.9 m, and the FUT was in a loose state of relative zero strain elsewhere.

3.4.4 Experimental results and discussion

3.4.4.1 OTDR-like trace

For long-range distributed sensing, good location accuracy is highly desired in addition to the high temperature and strain resolution detection of changes in environmental variables. Thus an OTDR-like trace is firstly acquired to locate temperature changing and strain applied positions on the optical fiber. The spatial resolution ΔZ is determined by the sweep frequency range ΔF, following the formula of $\Delta Z = c/(2n\Delta F)$, where c is the speed of light in vacuum and n is the group index of the fiber [50]. The theoretical spatial resolution for 5.9 nm swept range is calculated to be 0.14 mm.

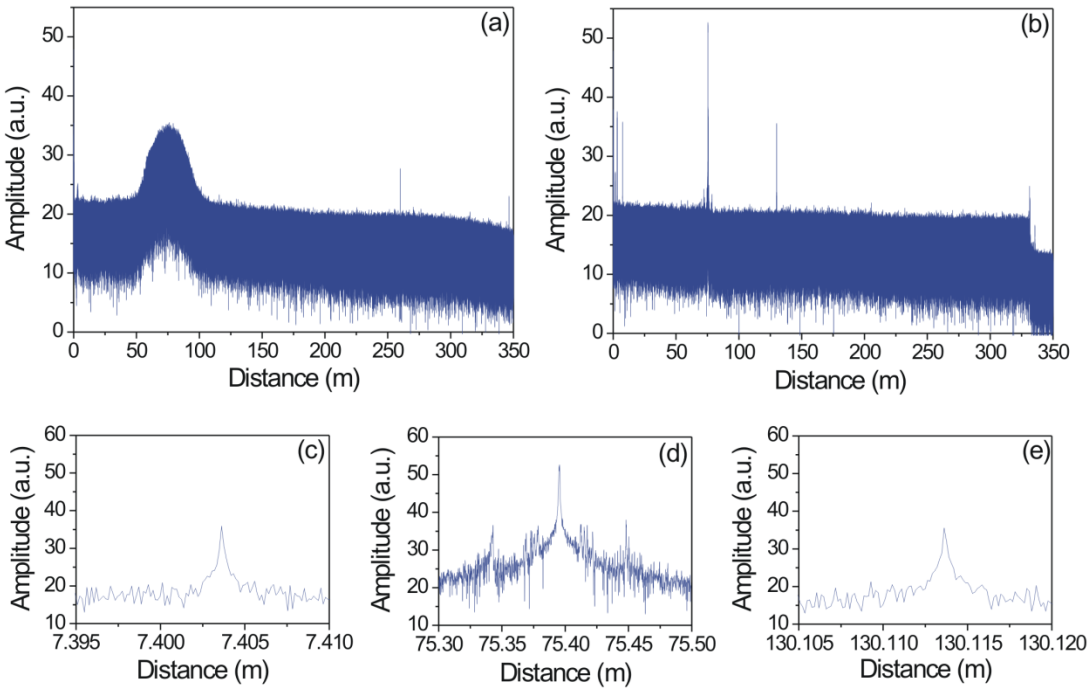

Fig. 3.11 OTDR-like traces (a) before and (b) after using cubic spline interpolation.

Fresnel reflection peaks corresponding to three connections at (c) 7.4 m with the first APC-APC connection, (d) 75.4 m with a PC-PC connection, and (e) 130 m with APC connection

Fig. 3.11 (a) and 3.11 (b) show the Rayleigh backscatter signals as a function of distance along the FUT with and without using the cubic spline interpolation, respectively. It is obvious that the OTDR-like trace has been tremendously improved through the cubic spline interpolation to increase the effective spatial resolution. In Fig. 3.11 (a), only one dominant Fresnel reflection peak is displayed at a rough location of the PC-PC connection and much positional information along the FUT is missing because of the relative low effective spatial resolution caused by the high nonlinearity of the TLS frequency scan. On the contrary, Fig. 3.11 (b) distinctly exhibits three Fresnel reflection peaks induced by the first APC-APC, the PC-PC, and the second APC-APC connections at the positions of 7.4 m, 75.4 m, and 130.1 m, respectively, which are undetectable without using interpolation. Figures 3(c-e) display true Fresnel reflection profiles of the above three connections, showing effective spatial resolution of 0.3 mm which is in excellent agreement with the calculated spatial resolution. Due to the high reflection as well as the PC reflector pair formed air cavity, some noise exists at the location of PC, therefore a larger distance window is adopted here to accommodate the complex signal occurring around the PC reflector, correspondingly leading to a larger division of the horizontal axis. The back reflection in the APC-APC connection is 17-dB less than that of the PC-PC connection, and the fiber knot at the fiber end is visible at 331 m with an 8-dB drop in the power, which validated a maximum ~300m sensing length. The spatial resolution

can be determined by half maximum at full width (HMFW) at arbitrary APC reflection point. In Fig. 3.11 (c) and (e), the spatial resolution is 0.14 mm at horizontal axe, where the HMFW consists of less than 2 sampling intervals (~0.28mm). Therefore a spatial resolution of less than 0.3mm is achieved. In addition, several other peaks are also observed before the first APC-APC connection induced by the internal reflection points.

3.4.4.2 Temperature and Strain Sensing Result

Figure 3.12 shows experimental results of wavelength shift as the temperature was increased from $30°C$ to $80°C$ with an increment step of $5°C$. A total of 500 and 2300 data points at the positions of 10.0 m and 84.5 m along the OTDR-like traces are used to calculate the cross-correlation and calibrate the wavelength shift accordingly, equivalent to spatial resolution of 7.0 cm and 32.2 cm according to $\Delta Z_{sensing}=\Delta Z*N$, where N is the number of data points and $\Delta Z_{sensing}$ the sensing spatial resolution. There is a difference between $\Delta Z_{sensing}$ and ΔZ as the cross-correlation demands enough spatial points to maintain calculation accuracy. Figure 3.12(a) presents wavelength shift of cross-correlation calculation with an increasing temperature along a section of fiber located at 10.0 m. The average wavelength shift is determined by averaging ten continuous points within the regions where the fiber was heated. Figure 3.12(b) shows the average wavelength shift linearly changes with temperature. The thermal sensitivity coefficients at 10.0 and 84.5 m based on linear regression are

$10.20\,pm/°C$ and $10.02\,pm/°C$, respectively. The errors at 10.0 and 84.5 m are calculated by taking the maximum error within the standard deviations from different temperatures to be 6.64 pm and 5.88 pm, which are converted to temperature accuracy of $0.65°C$ and $0.59°C$, respectively.

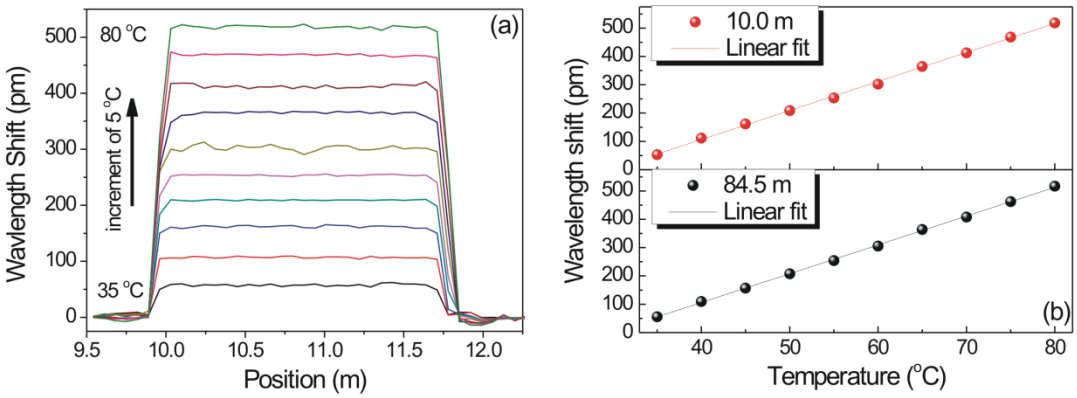

Fig. 3.12 (a) Wavelength shift of cross-correlation calculation along the fiber at different temperatures at 10.0 m. (b) Average wavelength shift as a function of temperature at (top) 10.0 m and (bottom) 84.5 m, respectively

Figure 3.13 shows the experimental results of the strain induced wavelength shift of cross-correlation calculation. In Fig. 3.13 (a), the wavelength shift under different strain, which was increased from 56.8 με to 227.2 με with an increment of 56.8 με, and from 227.2 με to 568.0 με with an increment of 113.6 με, is shown along the fiber at the position of 8.5 m with a length of 0.9 m. A total of 500 and 800 data points corresponding to strain spatial resolution of 7 cm and 11.2 cm are used to determine wavelength shifts at 8.5 m and 75.5 m. Fig. 3.13 (b) presents the average wavelength shift with respect to varying strain at 8.5 m and 75.5 m where linear regression is applied and the strain sensitivity coefficients are calculated to be 1.20 pm/με and 1.22 pm/με, respectively. The wavelength shift measurement errors at 8.5 m and 75.5 m are

1.82 pm and 2.80 pm, corresponding to strain accuracy of 1.5 με and 2.3 με, respectively.

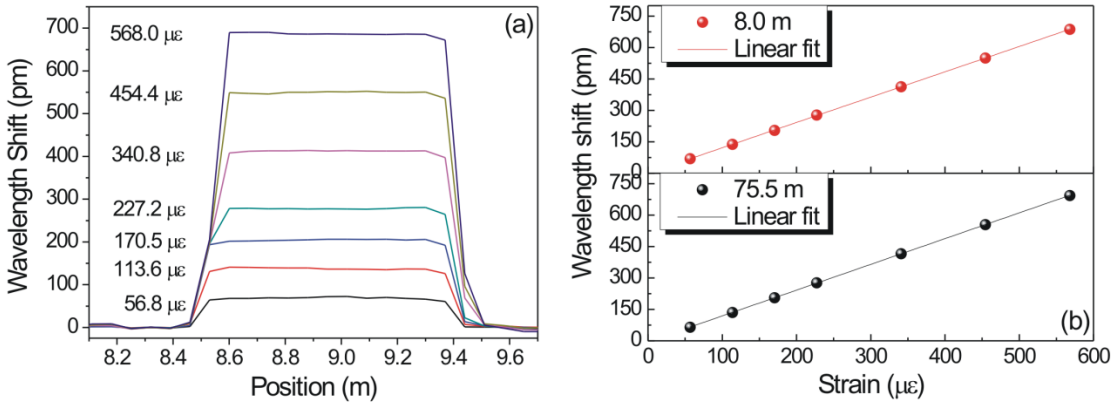

Fig. 3.13 (a) Wavelength shift of cross-correlation calculation along the fiber under different strain at 8.5 m. (b) Average wavelength shift as a function of strain at (top) 8.5 m and (bottom) 75.5 m, respectively

3.4.4.3 Spatial Resolution at different distances

In temperature and strain sensing experiments, it is found that the sensing resolution deteriorates as the fiber length extends. In order to determine the actual sensing resolution, the number of data points needed for obtaining an optimum cross-correlation figure with a minimum side peak suppression ratio of 2 is calculated. The cross-correlation figures at three different locations of 10 m, 140 m, and 310 m using 500, 2800, and 6000 data points in the temperature measurement are illustrated in Fig. 3.14, which indicates that the predicted temperature spatial resolution are about 7 cm, 39 cm and 84 cm, respectively, as shown in Figs. 3.14(a-c). In addition, the temperature spatial resolution at different locations (10, 50 and 150 m) along the FUT as a function of the wavelength tuning speed is shown in Fig. 3.15. It is found

that at the same locations a higher wavelength sweeping speed (e.g. 10 nm/s) requires more data points for cross-correlation compared to a lower wavelength sweeping speed (e.g. 6 or 8 nm/s), indicating reduced spatial resolution with increasing wavelength tuning speed.

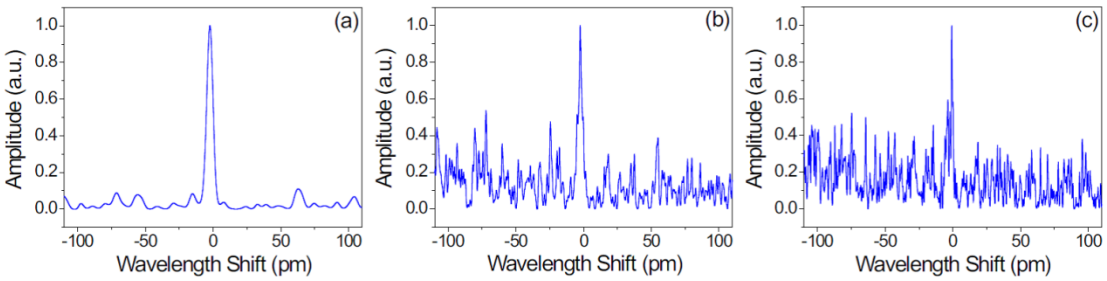

Fig. 3.14 Cross-correlation figures in the temperature measurement at three different locations of (a) 10 m with 7 cm resolution, (b) 140 m with 39 cm resolution, and (c) 310 m with 84 cm resolution

This spatial resolution deterioration effect can be explained in the following three aspects: Firstly, although the cubic spline interpolation can predict data points with relative high accuracy compared to other well-known algorithms, the prediction errors still exist in the resampled beat signal and accumulate at the far end of the FUT, leading to the deterioration in spatial resolution. Secondly, unlike the long range OFDR locating applications, temperature and strain sensing requires more accurate local Rayleigh backscattering profile to cipher precise wavelength shift value. However the increased phase noise at a longer distance may disturb the local spectrum and more data points are needed for cross-correlation to obtain a good signal of high SNR. Lastly, the linewidth of the TLS operating at the fast wavelength tuning speed of 5.9 nm/s (737 GHz/s frequency sweeping speed, equivalently) increases relative to the case of a low sweeping speed due to the increasing phase noise during

the lasing process, which leads to a reduced coherent length [71]. Therefore, one must carefully select an appropriate tuning speed in order to maintain the accuracy of Rayleigh backscattering profile. Although a smaller tuning speed can reduce the phase noise, the spatial resolution will correspondingly decrease given the fixed sampling points of the DAQ. Considering above factors, a ~300 m SMF is deliberately chosen for demonstration in this work.

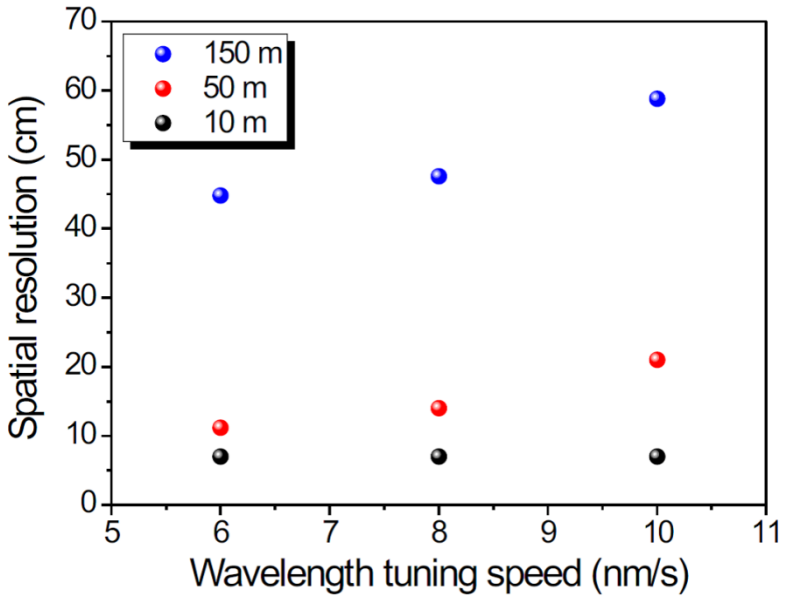

Fig. 3. 15 Temperature spatial resolution as a function of the wavelength tuning speed at different locations

In summary, distributed temperature and strain sensing are finally realized based on an OFDR system with a measurement length of more than 300 m by using a cubic spline interpolation algorithm which effectively compensates the frequency tuning nonlinearity of the TLS. The temperature and strain sensitivities are 10 pm/˚C and 1.2 pm/με, respectively, with measurement accuracies of 0.7 ˚C and 2.3 με at spatial resolution of 7 cm. The sensing resolution deteriorates at far distances due to increased phase noise from the laser tuning process. To further improve the sensing

distance and spatial resolution, one may use a TLS with a large tuning range and a slower tuning speed, and a DAQ card of a large on-board memory buffer combined with a powerful computer. The proposed technique enables an extended sensing distance with excellent spatial resolution, spectral sensitivity, and measurement accuracy over other traditional nonlinearly-triggered OFDR systems, and has great potential in a variety of practical sensing applications such as structural health monitoring of civil infrastructure systems.

Chapter 4

Enhanced Temperature Response Sensing based on OFDR

4.1 Review and Principle of temperature sensing

In this section we shall review the principles of temperature sensing using OFDR. As discussed in Chapter 2.2.3, OFDR detects the temperature, strain or any other environmental perturbations by measuring the local wavelength shift, where a number of spatial points are used for cross-correlation. A formula describing this relationship between wavelength shift and temperature change is given as follows [4]:

$$\Delta\lambda / \lambda = K_T \Delta T \tag{4.1}$$

where K_T is a thermal coefficient that describes the response of the fiber and consists of two terms [4]. The first term – thermal expansion coefficient α_Λ involves all materials that contribute to the fiber. Specifically, bare fiber made out of pure silica has a typical value of $\alpha_\Lambda = 0.55\times10^{-6}K^{-1}$[50]. When fiber is coated by acrylate ($\alpha_\Lambda = 40\times10^{-6}K^{-1}$), the thermal expansion coefficient is a weighted value of coating and bare fiber, which corresponds to a larger α_Λ. The second term – thermal optic coefficient α_n is defined by dn/dT which describes the refractive index change with respect to temperature. α_n is a constant for a given material and is regardless of waveguide shape with a typical value of $\alpha_n = 6.1\times10^{-6}K^{-1}$[50].Taking both α_Λ and

α_n into account, the thermal coefficient for SMF is $K_T = \alpha_\Lambda + \alpha_n \sim 7.0 \times 10^{-6} K^{-1}$. Thus a linear wavelength shift is expected at a moderate temperature range, while typical temperature response at 1550nm is $\Delta\lambda / T = K_T \lambda = 10.85 pm \bullet K^{-1}$.

The above analysis provides a potential approach to enhance the temperature response: either enhance thermal expansion coefficient or enhance thermal optic coefficient. In the next two sections, two approaches aiming at enhancing the temperature response are individually discussed.

4.2 Enhanced temperature sensitivity based on OFDR with SMF

4.2.1 Principle of enhancing temperature response

As stated in 4.1, the temperature response to two terms: thermal expansion coefficient α_Λ and thermal optic coefficient α_n. Since α_n is a constant for given material, the only possible approach to enhance temperature response is to enlarge α_Λ which is a weighed value of coating and bare fiber. Following this idea, a coating with large thermal expansion coefficient and thickness would potentially enhance α_Λ.

4.2.2 Experiment Set-up

Fig. 4.1 shows the experimental set-up to measure distributed Rayleigh backscattering light. The configuration of the OFDR system consists of a TLS (Newfocus TLB6600),

a main interferometer with a polarization beam splitter (PBS) based polarization diversity receiver, an auxiliary interferometer to trigger data acquisition and mitigate errors induced in laser tuning process, photo detectors (PDs) and a data acquisition (DAQ). One polarization controller (PC) within the main interferometer and another PC in front of the FUT are adopted to adjust light polarization states. An interference signal is from PBS to obtain a polarization-independent signal by calculating a vector sum of p- and s-components of the detected signals. The laser operates at 40nm/s tuning speed from 1550nm to 1582.45nm, with total 2.5M sampling points. The spatial resolution is 24.7um using Eq. (2.57) in Chapter 2.

A section of bare SMF is glued on acrylic plank at both ends using contact adhesive, which guarantees the bare fiber is tightly fixed. It should be noted that the acrylic plank functions like a “coating”, which contributes to the thermal expansion coefficient due to the large cross area of plank, which is a rectangular shape with a height of 4mm and length of 20mm

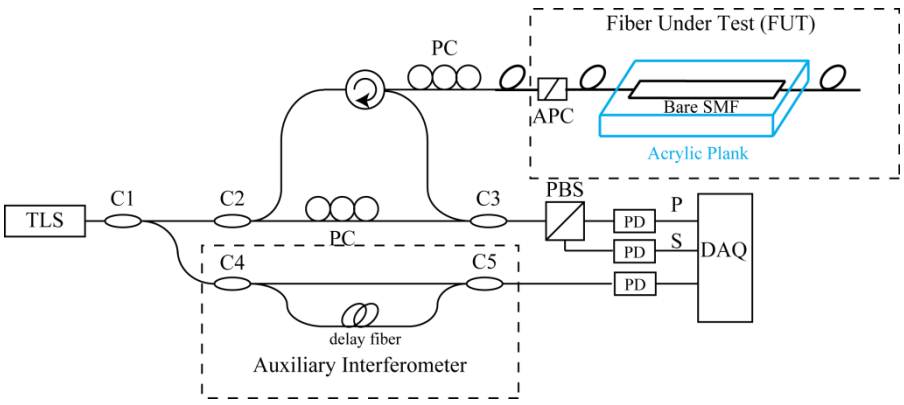

Fig. 4.1 The set-up of the OFDR system for SMF temperature measurement. TLS: tunable laser source; C1: 1:99 optical coupler; C2~C5: 50:50 optical coupler; PC: polarization controller; PBS: polarization beam splitter; PD: photodetector

4.2.3 Experimental Result and Discussion

To investigate the temperature response, the FUT was put into an oven and heated from 30°*C* to 50°*C* with 5°*C* temperature increment. A window of 12.4mm (~500 spatial points) is used to perform cross-correlation, a total 50 adjacent sensing points were calculated which covers the bare SMF with acrylic coating. Fig. 4.2 shows the distributed wavelength shift at different temperature. Two different type of acrylic (cast, extruded) with different thermal expansion coefficient were individually tested.

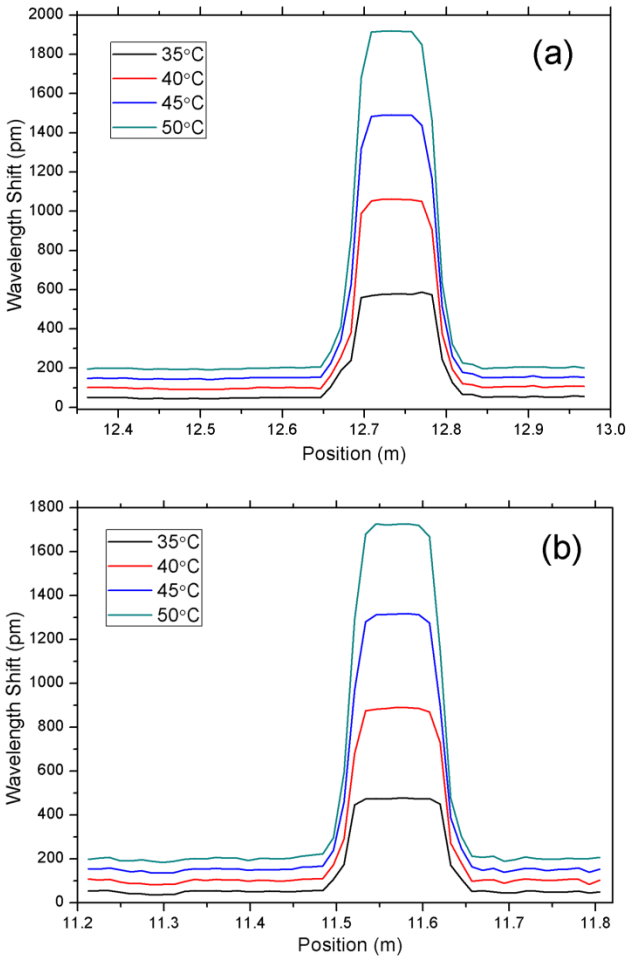

Fig. 4.2 Wavelength shift of cross-correlation calculation along FUT at different temperatures for (a) Acrylic, extruded (b) Acrylic, sheet, cast

We may notice from Fig. 4.2 (a) and (b) that there is apparently huge wavelength shift for the bared fiber glued to acrylic plank, when compared with SMF. This verifies the assumption that the overall temperature response is enhanced due to the acrylic "coating". The wavelength shift of the SMF and the acrylic "coating" bare fiber are individually calculated by averaging a certain length of points.

The average wavelength shift as a function of temperature for SMF (black dot), acrylic extruded coating (red dot) and acrylic cast (blue dot) are provided in following figure.

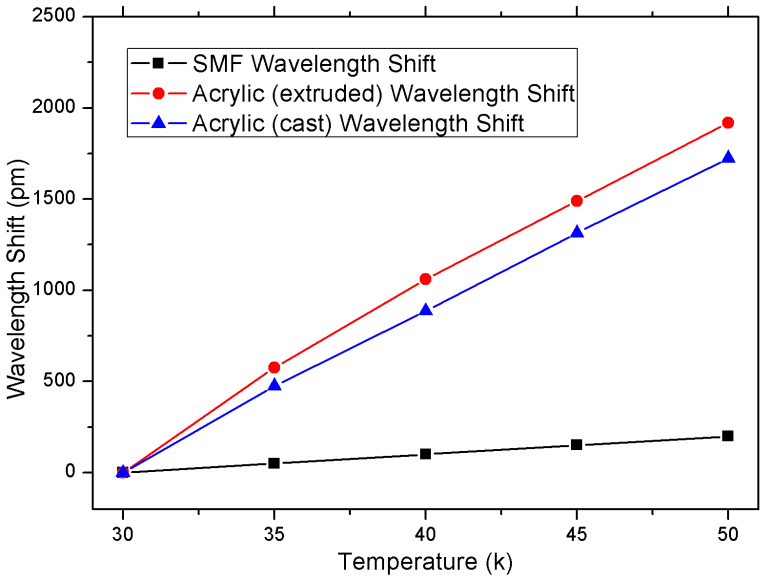

Fig. 4.3 Average wavelength shift as a function of temperature for SMF (black dot), acrylic extruded coating (red dot) and acrylic cast (blue dot)

Then a linear fitting is applied to the wavelength shift with respect to different temperature. Temperature response and coefficient of determination (R-square) are listed in following table:

Fiber coating types	Temperature Response	Adj. R-Square
Commercial SMF with coating	$10\,pm/K$	0.9999
Bare fiber glued on acrylic (extruded)	$95\,pm/K$	0.9943
Bare fiber glued on acrylic (cast, sheet)	$85.7\,pm/K$	0.9990

Table 4.1 Temperature response for different “coating” fiber

The above results indicate that the temperature response is tremendously enhanced for both acrylic extruded (~9.5times) and acrylic cast (~8.6 times) “coating” fiber. In other words, if the accuracy of SMF is 1˚C which corresponds to 10 pm wavelength resolution, the accuracy for acrylic extruded “coating” fiber is 9.5 times higher since the same wavelength resolution now indicates finer temperature increment (~0.1 ˚C). Similarly, if we keep the same temperature response, a higher spatial resolution is able to be obtained as fewer points are essential to ensure the wavelength resolution.

4.2.4 Thermal expansion coefficient measurement based on OFDR

Next we shall discuss the possibilities to use OFDR to measure the thermal expansion coefficient of solid material. As stated in Chapter 4.1, the temperature response is related with working wavelength as well as thermal coefficient, considering thermal coefficient is a summation of thermal expansion coefficient and thermal optic

coefficient, we have the following equation:

$$R_T = \lambda \bullet K_T = \lambda \bullet (\alpha_\Lambda + \alpha_n) \tag{4.2}$$

In this way, the thermal expansion coefficient can be calculated by:

$$\alpha_\Lambda = R_T / \lambda - \alpha_n \tag{4.3}$$

If we glue any solid material to fiber that function like a "coating", the solid material will contribute to thermal expansion coefficient since α_Λ is a weighted value of both coating and fiber. However, if the cross area of coating is much larger than that of fiber, α_Λ is approximately $\alpha_{\Lambda\_coating}$. Therefore, the thermal expansion coefficient could be determined.

Following this idea, we calculated α_Λ for both acrylic extruded and acrylic cast, with values of $55.2\times10^{-6} m/mK^{-1}$ and $49.2\times10^{-6} m/mK^{-1}$, respectively. In comparison, typical acrylic has a value of $72\times10^{-6} m/mK^{-1}$, which is slightly larger than the value of our approach. This is reasonable since the acrylic plank employed in this experiment is not thick enough to ignore fiber, resulting in a lower weighted value. Further works shall be done to increase the accuracy.

We proposed an approach to enhance the temperature response of OFDR by adding a "coating" with large thermal expansion coefficient. This large thermal expansion coefficient will contribute to overall thermal coefficient and therefore enhance the temperature response. Specifically, ~9.5 times and ~8.6 times higher temperature responses are achieved, using acrylic extruded and acrylic cast material as "coatings". To my knowledge, this is the first time an OFDR system is shown to perform high temperature accuracy sensing. Inversely, it is also possible to measure thermal

expansion coefficient of solid materials. Further experiments shall be done for more accurate results.

4.3 Taper based distributed temperature sensing using OFDR

4.3.1 Introduction and Properties of Taper

Taper is a unique structure which has been studied for over 20 years and is named for its reduced diameter at transition region with a taper like shape. Originally, taper is used in fiber optical couplers where two fibers put in parallel are uniformly stretched by flame or CO_2 laser scanning [72, 73]. Since 2000, taper structures are widely implemented in temperature, strain, displacement, humidity and vibration sensing [12, 74-78]. Tapering is a simple, efficient and low-cost technique to generate higher order modes which can be employed in sensing by building interferometer structure. Compared to other fiber sensors, taper has similar performance but are more easily fabricated.

Taper can be also implemented in distributed sensing if a uniform taper waist diameter is guaranteed. Recently, the thermal and mechanical properties of taper has been studied using OFDR system [35], in which work a ~500 times higher strain sensitivity is achieved using ~6μm diameter taper. Following this idea, a possible approach to enhance the temperature sensitivity is to convert the temperature measurement into strain measurement.

In laboratory, a taper is commonly fabricated either by electrical-arc fusing where a fusion splicer is employed, or by flame scanning where a stretching stage and scanning hydrogen flame are used. A difference between those two taper fabricating techniques is that the former one fabricates abrupt taper with steep slope and short taper length, while the latter one fabricates gentle taper with small taper angles and homogeneous long taper length. An illustration of the taper structure and an image of abrupt taper are provided in Fig. 4.4, as follows:

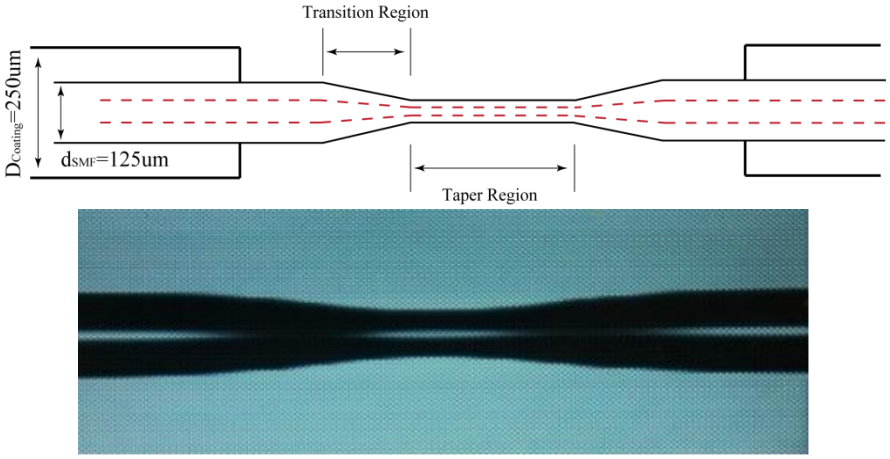

Fig. 4.4 (a) illustration of taper structure (b) actual image of abrupt taper fabricated by electrical-arc

Taper consists of two parts: transition region and taper region. Transition region is where low order mode (or core mode) being coupled to higher order modes (or cladding modes) due to field distribution mismatching. Taper region is a uniform region with a diameter as small as several micrometers where both core mode and cladding mode can propagate. It is noted that in gentle taper, small taper angle leads to almost no mode coupling as the slowly varying diameter guarantees no field distribution mismatching.

4.3.2 Principle of Enhanced temperature response using taper

In Chapter 4.2, we have proposed a SMF with acrylic "coating" has a temperature response which is ~9.5 times than that of SMF, in which experiment the thermal expansion coefficient is enhanced. Due to the fact that the diameter of taper is extremely small in our experiment (1μm), the ratio between the cross area of acrylic plank and the taper is much larger than that in Chap. 4.2. Therefore, the thermal expansion coefficient of the taper on acrylic coating could be ultimately close to that of acrylic coating, which is even larger than that in Chap. 4.2 and we could expect an even larger temperature response as $K_T = \alpha_\Lambda + \alpha_n$.

4.3.3 Experiment Set-up

Fig. 4.5 shows the experiment set-up to measure distributed Rayleigh backscattering light. The configuration of the OFDR system is quite similar with that in Chapter 4.2, except that the FUT is a taper with 1μm diameter: It consists of a TLS, a main interferometer with a polarization beam splitter (PBS) based polarization diversity receiver, an auxiliary interferometer to trigger data acquisition, photo-detectors (PD) and a data acquisition (DAQ). One polarization controller (PC) within the main interferometer and another PC in front of the FUT are adopted to adjust light polarization states. The PBS splits the interference signal into two orthogonal polarization states to obtain a polarization-independent signal by calculating a vector

sum of p- and s-components of the detected signals. The taper was drawn from SMF28 fiber with angled polish connector (APC) at both ends and is carefully put on a self-made sealed acrylic (extruded) stage, both ends of taper were glued to the stage which guaranteed the strain induced by acrylic stage was delivered to taper.

TLS operates at 40nm/s tuning speed from 1550nm to 1582.45nm, with total 2.5M sampling points. The spatial resolution is 24.7 μm using Eq. 2.57.

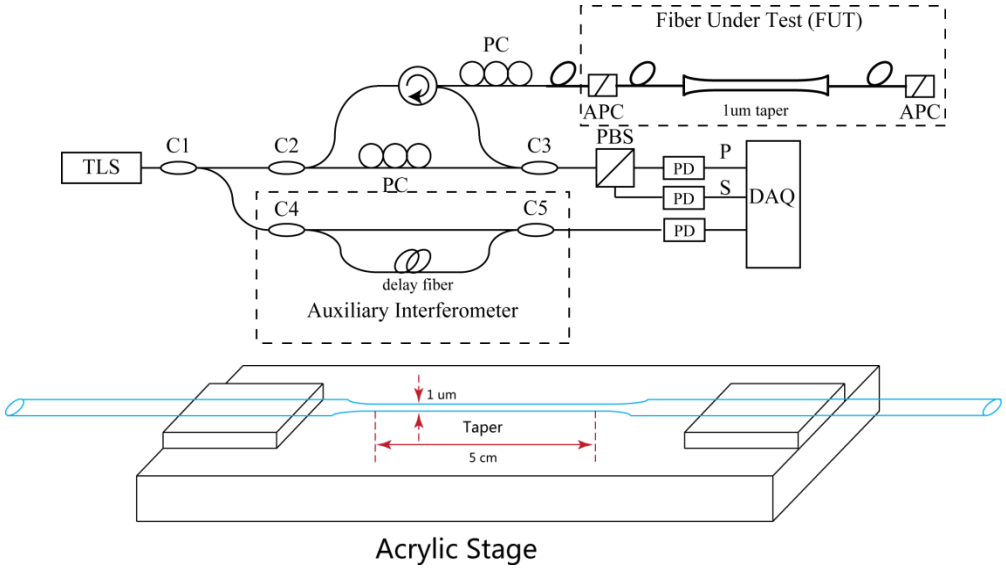

Fig. 4.5 (a) The configuration of the OFDR system for taper measurement and (b) Acrylic stage with taper

4.3.4 Experimental Result and Discussion

The distributed Rayleigh backscattering profile is shown in Fig. 4.6 within the taper region, the red line indicates the ideal diameter profile along the taper. A ~50dB increment in Rayleigh backscattering profile can be found within the taper region, which is even higher than the fiber end reflection. This huge improvement of Rayleigh backscatter is mainly induced by the inhomogeneity in waveguide structure.

For the taper with one micron diameter, any inhomogeneity induced by tapering process can affect the effective refractive index n_{eff} tremendously. The difference in n_{eff} between any two adjacent spatial points in taper leads to large backscattering due to this mismatching of n_{eff}, thus one can model the taper as a strong grating with random period.

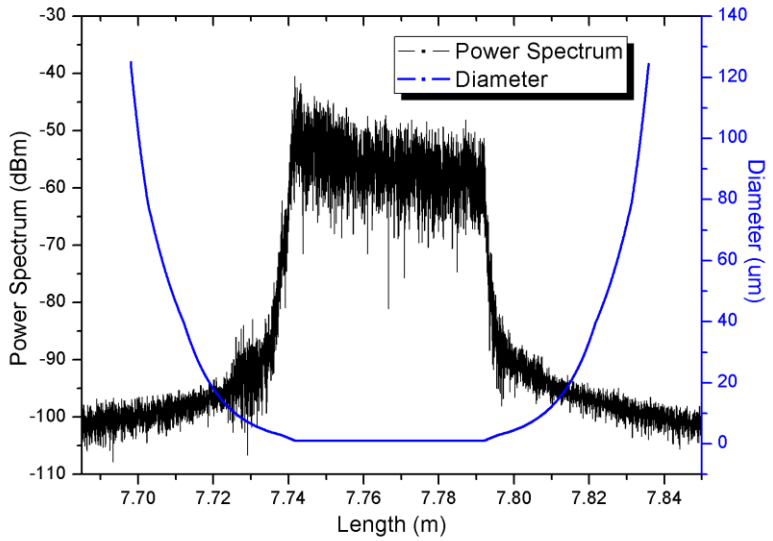

Fig. 4.6 Distributed Rayleigh backscattering profile within taper region (black line) and taper diameter along the fiber (blue line)

To investigate the thermal property of the compacted ultrathin taper, the taper was put into an oven and heated from $30°C$ to $80°C$ with $5°C$ increment. As shown in Fig. 4.7(a), a window of 3.7mm with 150 spatial points starting from 7.735m was selected and the correlations of 11 successive points are thereby calculated for different temperature. It is found that the central region of the taper provides flat wavelength shift to temperature, while both ends of the taper gives slightly higher

temperature sensitivity.

In order to verify the repeatability of the large wavelength shift, two tapers with 1 μm diameter are individually fabricated and tested. The average wavelength shift as a function of temperature for two tapers and SMF is experimentally demonstrated in Fig. 4.7(b). The wavelength shift is calculated by averaging all points within the taper region and linear fittings are applied. The calculated wavelength shift for the two tapers is $199.85\,pm/°C$ and $205.03\,pm/°C$, with a linearity of 99.1% and 98.8%, respectively. This result proves that in taper, both α_Λ and α_n are enhanced and the temperature response is 2 times of that in SMF with acrylic "coating".

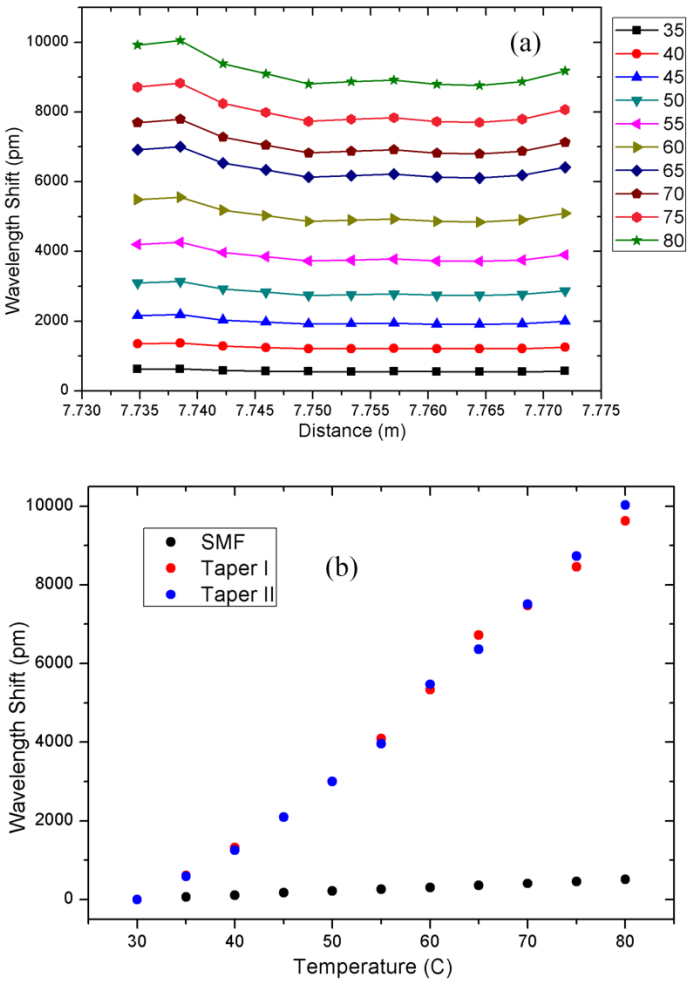

Fig. 4.7 (a) Wavelength shift of cross-correlation calculation along the fiber at different temperatures at 7.735m. (b) Average wavelength shift as a function of

temperature for 1um taper I (red dot), 1um taper II (blue dot) and SMF28 (black dot)

Although the temperature response is largely enhanced using taper with acrylic "coating", there are few limitations of taper in temperature sensing: Firstly, the 1 μm taper is difficult to fabricate and is fragile, a special holder must be made to protect the taper. Secondly, currently the length of taper cannot be made longer than 1 centimeter if the diameter is to be ~1 μm, therefore it is hard to use it as a real distributed sensor. Some further works regarding those limitations shall be done in the future.

In this section, we proposed a high sensitivity temperature sensor based on ultrathin fiber taper. The average temperature sensitivity of 1 μm taper is $200\,pm/°C$, which is almost 20 times the sensitivity of SMF. Temperature response was enhanced by increasing both α_Λ and α_n. The accuracy varies with the number of spatial points with a finest value of $0.026°C$.

Chapter 5

Summary and Future Works

5.1 Summary

In this thesis, we presented two major works aimed at improving the performance and applicability of OFDR: One aims at improving the sensing range while the other one aims at enhancing the temperature response.

Firstly, we proposed three novel algorithms (NU-FFT, Deskew filter, Cubic spline interpolation) to extend the working range of OFDR and an extended sensing range OFDR with good temperature and strain accuracies is achieved. This is also the first time an OFDR without triggered data acquisition is employed in distributed sensing. Compared with traditional nonlinear triggered OFDR, the new configuration achieved ~4 times (~300m) sensing range than the commercial one (~70m). More specifically, this new set-up is capable for sensing range as close as laser coherence length and demands no further components. Thus it is a practical tool for long range distributed sensing with high temperature and strain accuracy.

Secondly, the temperature response of sensing fiber is enhanced ~10 times (for acrylic plank holder) and ~20 times (for ultrathin taper on acrylic plank holder), compared with that of SMF. The principles behind this are to increase thermal coefficient which consists of thermal expansion coefficient and thermal optic coefficient. In this work, a

bare fiber is fixed on acrylic plank, due to the large thermal expansion coefficient of acrylic (~ $72\times10^{-6} m/mK^{-1}$), the weighted thermal expansion coefficient is tremendously enhanced which in turn results in a large temperature response. For ultrathin taper with 1μm diameter, thermal optic coefficient is enhanced due to the waveguide geometry deformation. Therefore, the taper is experiencing an even higher temperature response than bare fiber with acrylic "coating". This work is especially meaningful for its easy fabrication, low cost and extremely high temperature response and leads to practical usage for high accuracy distributed temperature sensing.

5.2 Future Works

In this thesis, we improved the performance of OFDR in two aspects: Extending the sensing range and enhancing the temperature response.

As the sensing range is primarily limited by TLS coherent length; one possible approach to further stretch the sensing range is to increase the laser coherence length. It is found that a TLS commonly has a longer coherence length if it works at a fairly high tuning speed [79]. Following this idea, one could possibly achieve longer sensing range and better spatial resolution by simply using high TLS tuning speed (~10nm/s or higher). In this way, a high speed DAQ is required in order to obtain the correct instant optical frequency of TLS, while maintaining other experiment set-up.

The temperature response is successfully enhanced in Chap. 4. However, the acrylic plank is not real "coating" since the bare fiber is not fully surrounded. Regarding this

issue, further experiments shall be using real coating where the bare fiber is uniformly coated.

Bibliography

1. X. Bao and L. Chen, "Recent Progress in Distributed Fiber Optic Sensors," Sensors **12**, 8601-8639 (2012).
2. M. A. Arnold, "Fiber-Optic Chemical Sensors," Analytical Chemistry **64**, 1015A-1025A (1992).
3. X. F. Huang, D. R. Sheng, K. F. Cen, and H. Zhou, "Low-cost relative humidity sensor based on thermoplastic polyimide-coated fiber Bragg grating," Sensors and Actuators B: Chemical **127**, 518-524 (2007).
4. A. Othonos, "Fiber Bragg gratings," Review of Scientific Instruments **68**, 4309-4341 (1997).
5. X. Dong, H. Y. Tam, and P. Shum, "Temperature-insensitive strain sensor with polarization-maintaining photonic crystal fiber based Sagnac interferometer," Applied Physics Letters **90**, 151113-151113-151113 (2007).
6. T. W. Kao and H. F. Taylor, "High-sensitivity intrinsic fiber-optic Fabry?Perot pressure sensor," Opt. Lett. **21**, 615-617 (1996).
7. T. Li, A. Wang, K. Murphy, and R. Claus, "White-light scanning fiber Michelson interferometer for absolute position?distance measurement," Opt. Lett. **20**, 785-787 (1995).
8. Y. Li, X. Wang, and X. Bao, "Sensitive acoustic vibration sensor using single-mode fiber tapers," Appl. Opt. **50**, 1873-1878 (2011).
9. P. Lu, L. Men, K. Sooley, and Q. Chen, "Tapered fiber Mach–Zehnder interferometer for simultaneous measurement of refractive index and temperature," Applied Physics Letters **94**, - (2009).
10. K. A. Murphy, M. F. Gunther, A. Wang, R. O. Claus, and A. M. Vengsarkar, "Extrinsic Fabry-Perot Optical Fiber Sensor," in *Optical Fiber Sensors*, Collected Papers of the International Conferences on Optical Fiber Sensors 1983-1997 (Optical Society of America, 1992), P30.
11. Z. L. Ran, Y. J. Rao, W. J. Liu, X. Liao, and K. S. Chiang, "Laser-micromachined Fabry-Perot optical fiber tip sensor for high-resolution temperature-independent measurement of refractive index," Opt. Express **16**, 2252-2263 (2008).
12. Z. Tian, S. S. H. Yam, and H.-P. Loock, "Refractive index sensor based on an abrupt taper Michelson interferometer in a single-mode fiber," Opt. Lett. **33**, 1105-1107 (2008).
13. T. Wei, Y. Han, H.-L. Tsai, and H. Xiao, "Miniaturized fiber inline Fabry-Perot interferometer fabricated with a femtosecond laser," Opt. Lett. **33**, 536-538 (2008).
14. M. G. Xu, J. L. Archambault, L. Reekie, and J. P. Dakin, "Discrimination between strain and temperature effects using dual-wavelength fibre grating sensors," Electronics Letters **30**, 1085-1087 (1994).
15. D.-P. Zhou, Z. Qin, W. Li, L. Chen, and X. Bao, "Distributed vibration sensing with time-resolved optical frequency-domain reflectometry," Opt. Express **20**, 13138-13145 (2012).
16. J. P. Dakin, D. J. Pratt, G. W. Bibby, and J. N. Ross, "Distributed optical fibre Raman temperature sensor using a semiconductor light source and detector," in *Electronics Letters,* (Institution of Engineering and Technology, 1985), pp. 569-570.
17. M. A. Farahani and T. Gogolla, "Spontaneous Raman Scattering in Optical Fibers with

Modulated Probe Light for Distributed Temperature Raman Remote Sensing," J. Lightwave Technol. **17**, 1379 (1999).

18. A. Fernandez Fernandez, P. Rodeghiero, B. Brichard, F. Berghmans, A. H. Hartog, P. Hughes, K. Williams, and A. P. Leach, "Radiation-tolerant Raman distributed temperature monitoring system for large nuclear infrastructures," Nuclear Science, IEEE Transactions on **52**, 2689-2694 (2005).
19. D. Hwang, D.-J. Yoon, I.-B. Kwon, D.-C. Seo, and Y. Chung, "Novel auto-correction method in a fiber-optic distributed-temperature sensor using reflected anti-Stokes Raman scattering," Opt. Express **18**, 9747-9754 (2010).
20. B. Gabriele, A. S. Marcelo, and P. Fabrizio Di, "Simultaneous distributed strain and temperature sensing based on combined Raman–Brillouin scattering using Fabry–Perot lasers," Measurement Science and Technology **21**, 094025 (2010).
21. Y. Dong, H. Zhang, L. Chen, and X. Bao, "2 cm spatial-resolution and 2 km range Brillouin optical fiber sensor using a transient differential pulse pair," Appl. Opt. **51**, 1229-1235 (2012).
22. Z. Zhang and X. Bao, "Distributed optical fiber vibration sensor based on spectrum analysis of Polarization-OTDR system," Opt. Express **16**, 10240-10247 (2008).
23. L. Yuelan, Z. Tao, C. Liang, and B. Xiaoyi, "Distributed Vibration Sensor Based on Coherent Detection of Phase-OTDR," Lightwave Technology, Journal of **28**, 3243-3249 (2010).
24. Q. Zengguang, Z. Tao, C. Liang, and B. Xiaoyi, "High Sensitivity Distributed Vibration Sensor Based on Polarization-Maintaining Configurations of Phase-OTDR," Photonics Technology Letters, IEEE **23**, 1091-1093 (2011).
25. X. Bao, D. J. Webb, and D. A. Jackson, "22-km distributed temperature sensor using Brillouin gain in an optical fiber," Opt. Lett. **18**, 552-554 (1993).
26. T. Kurashima, T. Horiguchi, and M. Tateda, "Distributed-temperature sensing using stimulated Brillouin scattering in optical silica fibers," Opt. Lett. **15**, 1038-1040 (1990).
27. X. Bao, D. J. Webb, and D. A. Jackson, "32-km distributed temperature sensor based on Brillouin loss in an optical fiber," Opt. Lett. **18**, 1561-1563 (1993).
28. R. Bernini, A. Minardo, and L. Zeni, "Distributed Sensing at Centimeter-Scale Spatial Resolution by BOFDA: Measurements and Signal Processing," Photonics Journal, IEEE **4**, 48-56 (2012).
29. W. Li, X. Bao, Y. Li, and L. Chen, "Differential pulse-width pair BOTDA for high spatial resolution sensing," Opt. Express **16**, 21616-21625 (2008).
30. W. Eickhoff and R. Ulrich, "Optical frequency domain reflectometry in single‐mode fiber," Applied Physics Letters **39**, 693-695 (1981).
31. S. T. Kreger, D. K. Gifford, M. E. Froggatt, B. J. Soller, and M. S. Wolfe, "High Resolution Distributed Strain or Temperature Measurements in Single- and Multi-Mode Fiber Using Swept-Wavelength Interferometry," in *Optical Fiber Sensors*, OSA Technical Digest (CD) (Optical Society of America, 2006), ThE42.
32. A. B. Am, D. Arbel, and A. Eyal, "OFDR with double interrogation for dynamic quasi-distributed sensing," Opt. Express **22**, 2299-2308 (2014).
33. T. Chen, Q. Wang, R. Chen, B. Zhang, K. P. Chen, M. Maklad, and P. R. Swinehart, "Distributed hydrogen sensing using in-fiber Rayleigh scattering," Applied Physics Letters **100**, - (2012).
34. W. Li, L. Chen, and X. Bao, "Compensation of temperature and strain coefficients due to local

birefringence using optical frequency domain reflectometry," Optics Communications **311**, 26-32 (2013).

35. X. Wang, W. Li, L. Chen, and X. Bao, "Thermal and mechanical properties of tapered single mode fiber measured by OFDR and its application for high-sensitivity force measurement," Opt. Express **20**, 14779-14788 (2012).
36. X. Wang, G. Niedermayer, G. Lin, P. Lu, B. Wang, L. Chen, and X. Bao, "Polarization-maintaining property of tapered polarization-maintaining fibers," Appl. Opt. **52**, 1550-1554 (2013).
37. W. Xiaozhen, L. Wenhai, C. Liang, and B. Xiaoyi, "Distributed Mode Coupling Measurement Along Tapered Single-Mode Fibers With Optical Frequency-Domain Reflectometry," Lightwave Technology, Journal of **30**, 1499-1508 (2012).
38. I. Luna, Optical backscatter reflectometer (Model OBR 4600), "http://lunainc.com/wp-content/uploads/2012/11/NEW-OBR4600_Data-Sheet_Rev-04.pdf" (2014), retrieved.
39. R. W. Boyd, *Nonlinear Optics, 3rd ed.* (2008).
40. M. K. Barnoski, M. D. Rourke, S. M. Jensen, and R. T. Melville, "Optical time domain reflectometer," Appl. Opt. **16**, 2375-2379 (1977).
41. Y. Dong, L. Chen, and X. Bao, "Extending the Sensing Range of Brillouin Optical Time-Domain Analysis Combining Frequency-Division Multiplexing and In-Line EDFAs," J. Lightwave Technol. **30**, 1161-1167 (2012).
42. K. Shimizu, T. Horiguchi, Y. Koyamada, and T. Kurashima, "Coherent self-heterodyne detection of spontaneously Brillouin-scattered light waves in a single-mode fiber," Opt. Lett. **18**, 185-187 (1993).
43. M. Höbel, J. Ricka, M. Wüthrich, and T. Binkert, "High-resolution distributed temperature sensing with the multiphoton-timing technique," Appl. Opt. **34**, 2955-2967 (1995).
44. P. Jonghan, G. Bolognini, L. Duckey, K. Pilhan, C. Pilki, F. Di Pasquale, and P. Namkyoo, "Raman-based distributed temperature sensor with simplex coding and link optimization," Photonics Technology Letters, IEEE **18**, 1879-1881 (2006).
45. Z. Qin, L. Chen, and X. Bao, "Continuous wavelet transform for non-stationary vibration detection with phase-OTDR," Opt. Express **20**, 20459-20465 (2012).
46. J. C. Juarez and H. F. Taylor, "Polarization discrimination in a phase-sensitive optical time-domain reflectometer intrusion-sensor system," Opt. Lett. **30**, 3284-3286 (2005).
47. J. Li, Z. Wang, L. Zhang, F. Peng, S. Xiao, H. Wu, and Y. Rao, "124km phase-sensitive OTDR with Brillouin amplification," in 2014), 91575Z-91575Z-91574.
48. T. Zhu, Q. He, X. Xiao, and X. Bao, "Modulated pulses based distributed vibration sensing with high frequency response and spatial resolution," Opt. Express **21**, 2953-2963 (2013).
49. U. Glombitza and E. Brinkmeyer, "Coherent frequency-domain reflectometry for characterization of single-mode integrated-optical waveguides," Lightwave Technology, Journal of **11**, 1377-1384 (1993).
50. B. Soller, D. Gifford, M. Wolfe, and M. Froggatt, "High resolution optical frequency domain reflectometry for characterization of components and assemblies," Opt. Express **13**, 666-674 (2005).
51. Y. Koshikiya, F. Xinyu, and F. Ito, "Long Range and cm-Level Spatial Resolution Measurement Using Coherent Optical Frequency Domain Reflectometry With SSB-SC Modulator and Narrow Linewidth Fiber Laser," Lightwave Technology, Journal of **26**, 3287-3294 (2008).

52. T.-J. Ahn, J. Y. Lee, and D. Y. Kim, "Suppression of nonlinear frequency sweep in an optical frequency-domain reflectometer by use of Hilbert transformation," Appl. Opt. **44**, 7630-7634 (2005).
53. F. Ito, X. Fan, and Y. Koshikiya, "Long-Range Coherent OFDR With Light Source Phase Noise Compensation," J. Lightwave Technol. **30**, 1015-1024 (2012).
54. R. G. S. M. Froggatt, and D. K. Gifford,, "High resolution interferometric optical frequency domain reflectometry (OFDR) beyond the laser coherence length," (2007).
55. S. Vergnole, D. Lévesque, and G. Lamouche, "Experimental validation of an optimized signal processing method to handle non-linearity in swept-source optical coherence tomography," Opt. Express **18**, 10446-10461 (2010).
56. K. Yuksel, M. Wuilpart, and P. Mégret, "Analysis and suppression of nonlinear frequency modulation in an optical frequency-domain reflectometer," Opt. Express **17**, 5845-5851 (2009).
57. Z. Ding, T. Liu, Z. Meng, K. Liu, Q. Chen, Y. Du, D. Li, and X. S. Yao, "Note: Improving spatial resolution of optical frequency-domain reflectometry against frequency tuning nonlinearity using non-uniform fast Fourier transform," Review of Scientific Instruments **83**, - (2012).
58. Z. Ding, X. S. Yao, T. Liu, Y. Du, K. Liu, J. Jiang, Z. Meng, and H. Chen, "Compensation of laser frequency tuning nonlinearity of a long range OFDR using deskew filter," Opt. Express **21**, 3826-3834 (2013).
59. E. D. Moore and R. R. McLeod, "Correction of sampling errors due tolaser tuning rate fluctuations inswept-wavelength interferometry," Opt. Express **16**, 13139-13149 (2008).
60. O. Y. Sagiv, D. Arbel, and A. Eyal, "Correcting for spatial-resolution degradation mechanisms in OFDR via inline auxiliary points," Opt. Express **20**, 27465-27472 (2012).
61. A. Dutt and V. Rokhlin, "Fast Fourier Transforms for Nonequispaced Data," SIAM Journal on Scientific Computing **14**, 1368-1393 (1993).
62. L. Greengard and J. Lee, "Accelerating the Nonuniform Fast Fourier Transform," SIAM Review **46**, 443-454 (2004).
63. K. K. H. Chan and S. Tang, "High-speed spectral domain optical coherence tomography using non-uniform fast Fourier transform," Biomed. Opt. Express **1**, 1309-1319 (2010).
64. K. Zhang and J. U. Kang, "Graphics processing unit accelerated non-uniform fast Fourier transform for ultrahigh-speed, real-time Fourier-domain OCT," Opt. Express **18**, 23472-23487 (2010).
65. M. Burgos-Garcia, C. Castillo, S. Llorente, J. M. Pardo, and J. C. Crespo, "Digital on-line compensation of errors induced by linear distortion in broadband LFM radars," Electronics Letters **39**, 116-118 (2003).
66. A. Meta, P. Hoogeboom, and L. P. Ligthart, "Range Non-linearities Correction in FMCW SAR," in *Geoscience and Remote Sensing Symposium, 2006. IGARSS 2006. IEEE International Conference on*, 2006), 403-406.
67. R. S. G. W. G. Carrara, and R. M. Majewski, *Spotlight Synthetic Aperture Radar* (1995).
68. M. Unser, "Splines: a perfect fit for signal and image processing," Signal Processing Magazine, IEEE **16**, 22-38 (1999).
69. C. d. Boor, "A Practical Guide to Splines," (1978).
70. Wikipedia, "http://en.wikipedia.org/wiki/Spline_interpolation" (2014), retrieved.
71. R. Passy, N. Gisin, J. P. Von der Weid, and H. H. Gilgen, "Experimental and theoretical

investigations of coherent OFDR with semiconductor laser sources," Lightwave Technology, Journal of **12**, 1622-1630 (1994).

72. T. A. Birks and Y. W. Li, "The shape of fiber tapers," Lightwave Technology, Journal of **10**, 432-438 (1992).
73. J. M. Ward, D. G. O'Shea, B. J. Shortt, M. J. Morrissey, K. Deasy, and S. G. Nic Chormaic, "Heat-and-pull rig for fiber taper fabrication," Review of Scientific Instruments **77**, - (2006).
74. C. Bariáin, I. R. Matías, F. J. Arregui, and M. López-Amo, "Optical fiber humidity sensor based on a tapered fiber coated with agarose gel," Sensors and Actuators B: Chemical **69**, 127-131 (2000).
75. K. Q. Kieu and M. Mansuripur, "Biconical Fiber Taper Sensors," Photonics Technology Letters, IEEE **18**, 2239-2241 (2006).
76. Z. Shan, P. Fufei, and W. Tingyun, "Single-mode tapered optical fiber for temperature sensor based on multimode interference," in *Communications and Photonics Conference and Exhibition, 2011. ACP. Asia*, 2011), 1-6.
77. T. Zhaobing and S. S. H. Yam, "In-Line Abrupt Taper Optical Fiber Mach–Zehnder Interferometric Strain Sensor," Photonics Technology Letters, IEEE **21**, 161-163 (2009).
78. T. Zhaobing, S. S. H. Yam, J. Barnes, W. Bock, P. Greig, J. M. Fraser, H. Loock, and R. D. Oleschuk, "Refractive Index Sensing With Mach–Zehnder Interferometer Based on Concatenating Two Single-Mode Fiber Tapers," Photonics Technology Letters, IEEE **20**, 626-628 (2008).
79. N. P. TLB6600, "http://www.newport.com/TLB-6600-Venturi-Swept-Wavelength-Tunable-Lasers/917229/1033/info.aspx", retrieved.

Curriculum Vitae

Full name Jia Song

Education

M.Sc. (Sep.2012-Aug. 2014)
Department of Physics
University of Ottawa, Ottawa, Canada
Supervisors: Prof. Xiaoyi Bao

B.S. (Sep.2008-Jun.2012)
College of Precision Instruments and Opto-electronics Engineering
Tianjin University, Tianjin, P. R. China

Publications

Journal Papers

[1] **Jia Song**, Wenhai Li, Ping Lu, Yanping Xu, Liang Chen, and Xiaoyi Bao, “Long-range high spatial resolution distributed temperature and strain sensing based on optical frequency-domain reflectometry”, ***Photonics Journal***, 2014.2320742.

[2] Chams Baker, Yang Lu, **Jia Song**, and Xiaoyi Bao, “Incoherent optical frequency domain reflectometry based on a Kerr phase-interrogator”, ***Optics Express***, accepted.

Conference Papers

[1] Ping Lu, **Jia Song**, Liang Chen, and Xiaoyi Bao, “Tapered polarization-maintaining fiber sensor based on analysis of polarization evolution”, ***OFS 2014 conference paper***, accepted.

[2] Yanping Xu, Ping Lu, **Jia Song**, Liang Chen, Xiaoyi Bao, "Discrimination of temperature and axial strain using dispersion effects of high-order-mode fibers," SENSORS, 2013 IEEE , vol., no., pp.1,4, 3-6 Nov. 2013